Imperial College London

IMPERIAL COLLEGE LONDON

Faculty of Engineering

Department of Civil and Environmental Engineering

Topology Optimisation of Beam-to-Column Joints for Additive Manufacturing

Minze Zhang

2020-2021

Submitted in fulfilment of the requirements for the MSc and the Diploma of Imperial College London

DECLARATION OF OWN WORK

Declaration:

This submission is my own work. Any quotation from, or description of, the work of others is acknowledged herein by reference to the sources, whether published or unpublished.

Signature : Minze Zhang

CATALOGUE

ABSTRACT

Nowadays, additive manufacturing (AM) as a fundamental part of the automated manufacturing procedures, is applied to different industries, including automotive and aerospace manufacturing industries. Because of the limitation of the 3D printer and the lack of understanding of the printed material property, the application of AM in the construction industry falls behind other industries. Lacking the relevant standard also prevents the massive application of AM in construction.

To contribute to the promotion of the application of AM in construction, this research dissertation is carried on. This research project focuses on the topology optimisation of the steel beam-to-column joints and the assessment of the structural performance of the optimised joints. During the research, the influence of the topology optimisation setups is explored by comparison of the selected structural performance variables between the benchmark joint and the optimised joints.

After this research, these setups are classified into insignificant ones, such as the existent of column stiffeners, and the significant ones, such as the mesh size and the optimisation target. The most optimised joint, FJ-1013C-LC, is found, by the evaluation of twenty-seven optimised joints. This optimised joint deserves further analysis in future research project.

Key words: fine element model, topology optimisation, nonlinear analysis, beam-to-column joint, structural performance

TABLE OF CONTENTS

Figures:

Tables:

1. INTRODUCTION

This research project aims to investigate the structural performance of beam-to-column joints (Figure. 1), which is optimised by topology optimisation and predetermined to be fabricated by WAAM. The current research achievements of additive manufacturing, wire and arc additive manufacturing, and topology optimisation are collected through literature review and introduced in this section.

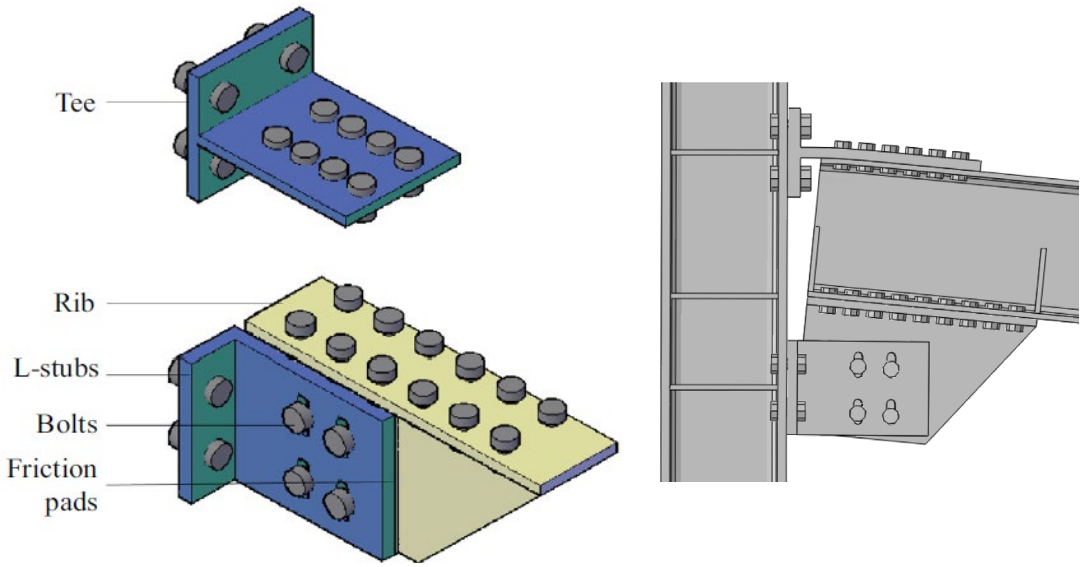

Figure. 1 A beam-to-column joint example (Tartaglia et al., 2021)

Additive manufacturing (AM), also known as 3D printing, is an automated manufacturing methodology, utilising the data from computer aid design (CAD) models. Compared with subtractive manufacturing methodologies, materials are added layer upon layer to form a 3D solid object (American Society for Material and Testing, 2012). AM can be embedded smoothly in the automatic fabrication process, acting as the subsequent step of the CAD model establishment. Hence, AM is becoming a vital production methodology in various fields such as electronic and medical device fabrication, automotive and aerospace manufacturing industries, artwork design. However, there are some disparities between the practical applications of construction and the fields previously mentioned (Wu, Wang & Wang, 2016). For example, the MX3D bridge (Figure. 2), the first 3D-printed steel bridge in the world, is manufactured in 2017 by 3D printing company MX3D (Hayley, 2017). Conventional manufacturing methodology is still widely adopted in construction. For example, the work of steel reinforcement arrangement and the on-site bolt assembly has often applied this method, as this work is inconvenient to be completed by machines automatically.

Figure. 2 The MX3D bridge (Buchanan & Gardner, 2019)

With the application of building information models (BIM), 3D models start to replace the 2D drawings during the structural design phase. These models can be easily exported and utilised for 3D printing. Hence, AM has huge potential and bright prospects in construction. With the increase in research achievements in AM, 3D printing starts to be adopted in concrete metal structure construction and brings various benefits to the construction industry.

In concrete construction, concrete structures (Figure. 3), fabricated by AM technique in factories, offer a lot of advantages to the construction industry. For concrete curing, the quality control is more effortless under the workshop environment than that under the on-site environment. In addition to material quality, the structural component quality can also be guaranteed since these components are fabricated automatically. In other words, the accident caused by human error can be prevented greatly by reducing labour work requirements (Bos et al., 2016). If the dimension of concrete members is similar, these members can be printed by several printers at the same time to reduce the construction time and to increase the construction efficiency. However, researchers focussed on printing plain concrete. Printing concrete within the framework of steel reinforcement is not explored in much detail.

(a) (b)

Figure. 3 (a) 3D printed concrete bridge (Buchanan & Gardner, 2019), (b) 3D printed artwork (Bos et al., 2016)

In steel construction, the application prospects of AM are brighter, as single material is used in the fabrication process. For example, AM is used to produce the nodes of a tensegrity structure by Arup (Figure. 4) (Galjaard, Hofman & Ren, 2015). When AM is used to produce metal connections, the material can be printed on a profile steel (Figure. 5) and connected with another profile steel by fasteners. Hence, the on-site weld can be omitted, and physical labour work is mainly limited to assembly bolts which can reduce the construction error and time. Apart from quality control, unused material can be recycled and reused to decrease the carbon footprint in the fabrication process. Hence, material consumption can be reduced compared with subtractive manufacturing. Architectural freedom can be maximised since AM can be used to produce more complex components. However, the cost of fabricating a component by AM is higher than that of producing the same volume of profile steel. The material property of printed components may be anisotropic, which differs from the material property of profile steel. For example, the printed stainless steel is an anisotropic material (Kyvelou et al., 2020).

(a) (b) (c)

Figure. 4 Comparison between (a) the conventional node and (b & c) two 3D printed optimised nodes (Galjaard et al., 2015)

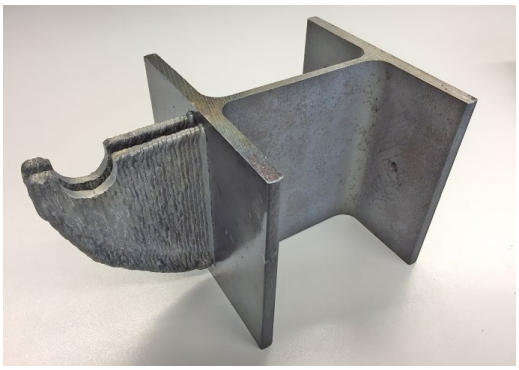

Figure. 5 3D printed hook on the I-shape column (Feucht, Lange & Erven, 2019)

Metal 3D printing technique contains four methods, sheet lamination, electrochemical addictive manufacturing (ECAM), powder bed fusion (PBF) and directed energy deposition (DED) (Buchanan & Gardner, 2019). Each method has its unique advantages and shortages, besides the general advantages and disadvantages mentioned

in the previous paragraph.

Sheet lamination (Figure. 6) is a method to laminate cross-section layers together (Gao et al., 2015). When this method is applied, not only the printed components can have high strength and a good surface finish, but the manufacturing cost is low (Gao et al., 2015). The complicity of components is limited by the thickness of the individual layer (Jared et al., 2017).

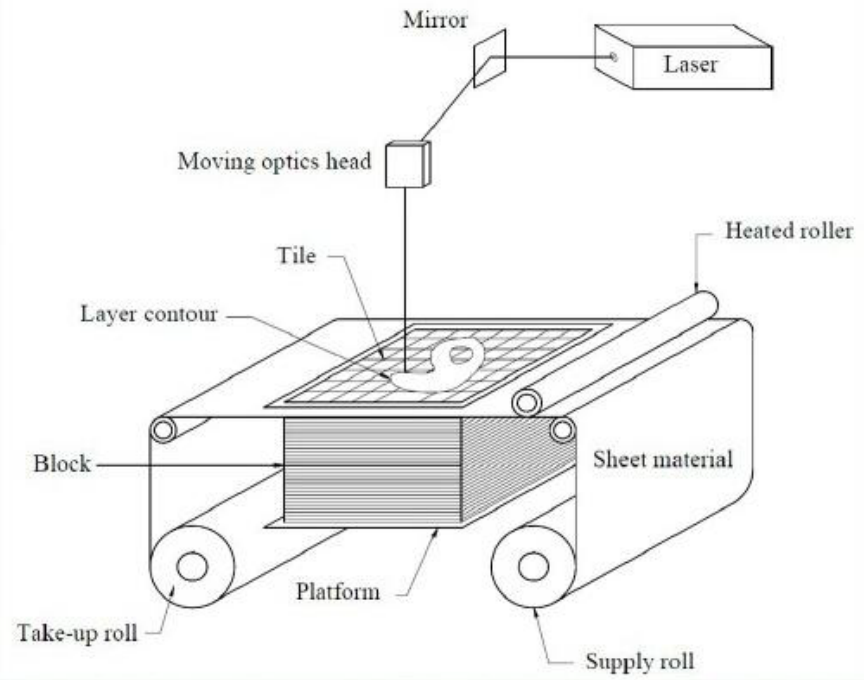

Figure. 6 Overview of the sheet lamination method (Bogue, 2014)

Electrochemical addictive manufacturing (ECAM) (Figure. 7) is excluded from ASTM F2792-12a (American Society for Material and Testing, 2012). This method is under the early research stages and can produce components at the atomic level using a similar fabrication process to electroplate. Hence, this method is only suitable for tiny components. Without the thermal process during production, internal residual stresses are not the principal consideration (Sundaram, Kamaraj & Kumar, 2015).

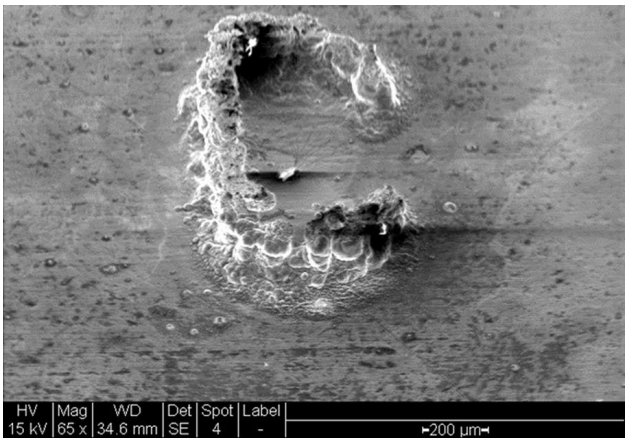

Figure. 7 SEM image of a component by ECAM (Sundaram, Kamaraj & Kumar, 2015)

Powder bed fusion (PBF) (Figure. 8) is a method to selectively fuse powder form of material under external energy from either a laser or electron beam. When this method is adopted, the manufacturing period of one component is considerably long. Only small components with complicated geometries are suitable to produce by this method (Williams et al., 2016). But the surface roughness is controlled to below 20 μm typically (Gu et al., 2012).

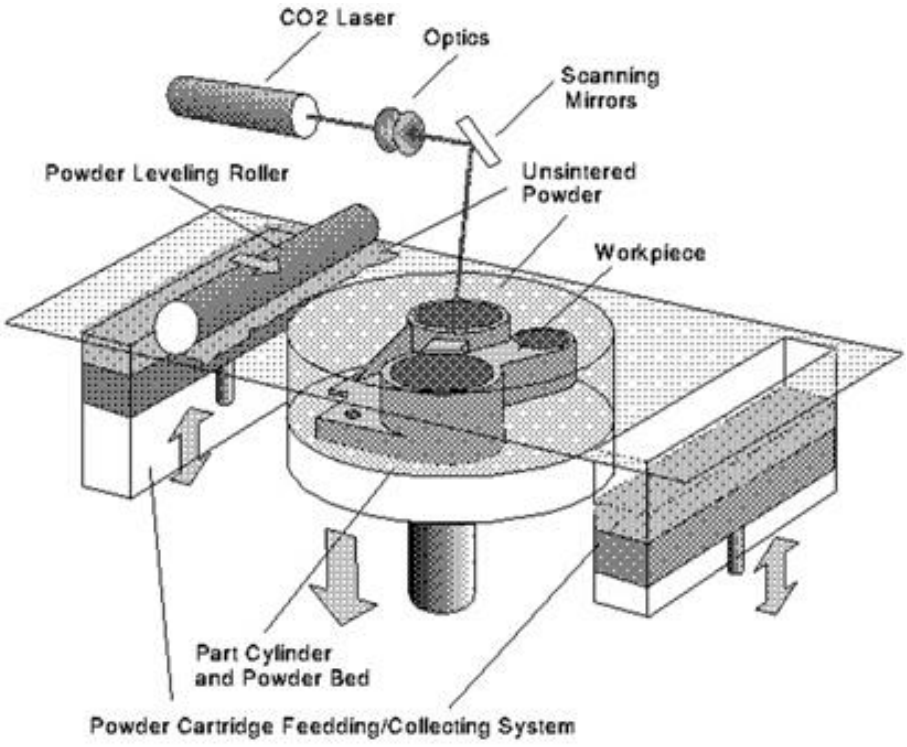

Figure. 8 Overview of PBF (Bogue, 2014)

Directed energy deposition (DED) (Figure. 9) is a method to selectively deposit material by melting metal under external energy from a laser or electron beam or plasma arc (Gao et al., 2015). Two forms of material can be used in DED, metal powder and wire. According to the form of metal material, DED can be divided into two sub-methods. When the metal powder is adopted, the printed components can have high complexity and low surface roughness (Gao et al., 2015). Like PBF, the scale of components is limited, and the manufacturing period is long. When the metal wire is adopted, DED can be referred to as wire and arc additive manufacturing (WAAM). The detail of WAAM is described in the following paragraphs.

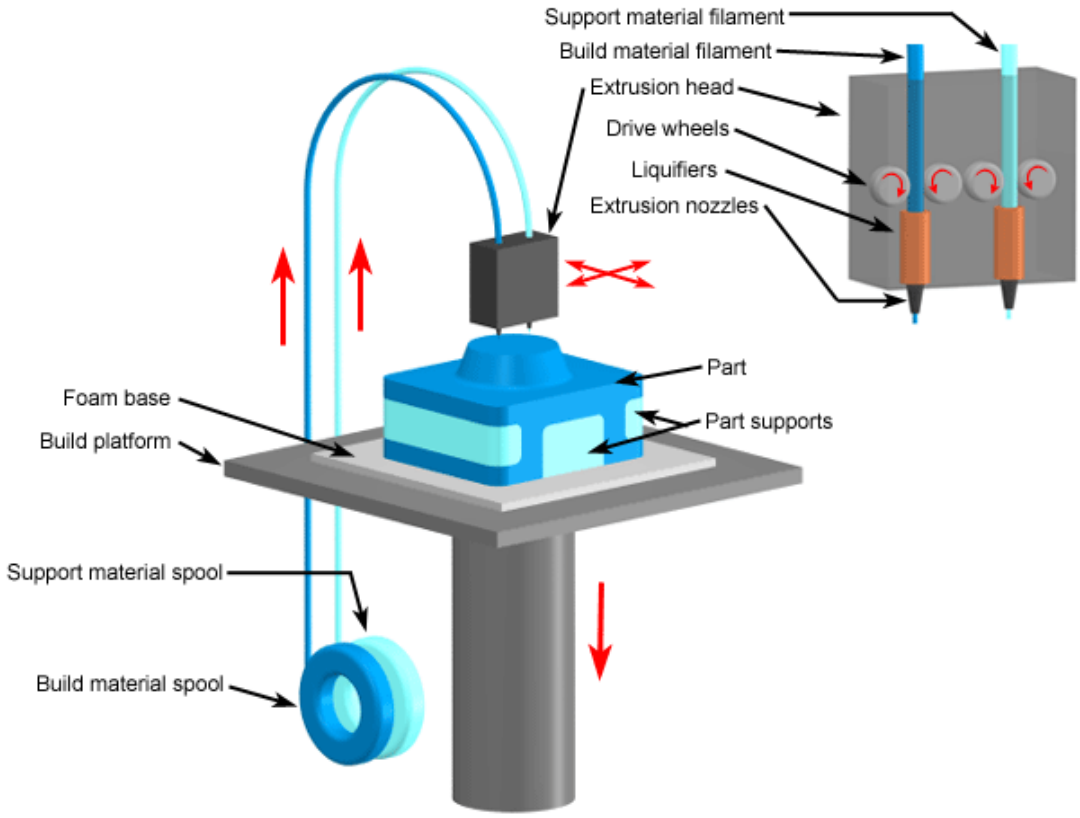

Figure. 9 Overview of DED based on wire form material (Bogue, 2014)

Research into the wire and arc additive manufacturing method has a long history. The first patent for WAAM was applied in 1926 (Joosten, 2015), and the study of WAAM has gained momentum since the 1990s. Based on the DED method, this method can utilise arc welding techniques to selectively deposit metal wire. These welding techniques mainly include plasma arc welding (PAW), gas metal arc welding (GMAW), and gas tungsten arc welding (GTAW) (Ding et al., 2015). MX3D bridge is fabricated by WAAM (Hayley, 2017). Differing from powder-based DED, WAAM can manufacture components with a high speed and low cost, but almost without scale limitation (Thompson et al., 2016; Williams et al., 2016).

Four main drawbacks that prevent the massive application of WAAM in steel construction. Firstly, the surface roughness (Figure. 10) is higher than that fabricated by other AM methods, affecting the component's appearance and making the as-built components unsuitable to be used as artwork (Williams et al., 2016). Although surface polish of as-built components can solve this issue, some new side effects may be caused, such as the increase in fabrication cost. Secondly, due to the limitation of the current equipment technique, the minimum thickness of components is limited to 2 to 3 mm. Additionally, as the material is molten due to thermal energy and settled to the selected position, the internal residual stresses become the primary issue to be considered during the fabrication process. Symmetrical movement of nozzle outwards from a central line,

symmetrical, simultaneous and back-to-back fabrication of two individual components, and heat treatment are three approaches to minimise side effects from these residual stresses (Williams et al., 2016).

Figure. 10 As-printed components by WAAM and without surface polish (Buchanan & Gardner, 2019)

The last drawback is that the as-built material property is anisotropic, like timber, which can be a characteristic of 3D printed metal components (Laghi et al., 2020; Tolosa et al., 2010). Even for powder-based DED, the same issue occurs on the as-built components with or without surface polish. The differences can be found in material characteristics, such as ultimate strength, ultimate strain and elastic modulus, and can be affected by the base material, the printing strategies and the angle between external loading direction and the deposition layer (Laghi et al., 2020). These differences are insignificant for printed carbon steel, which makes the isotropic material assumption rational. Hence, designers need to give sufficient consideration to the selection of base material, the determination of printing strategies and the simulation of the as-built components. The most common metal material in construction is carbon steel, and WAAM is more suitable for the construction industry to print large-scale components. A mass of research has begun to study the application and the structural performance of carbon steel components fabricated by WAAM. 3D printed components, such as stiffeners (Figure. 11 (a)), beam hooks (Figure. 5) and connection (Figure. 11 (b)), and even 3D printed bridges are under investigation (Buchanan & Gardner, 2019; Feucht, Lange & Erven, 2019; Hayley, 2017).

(a)

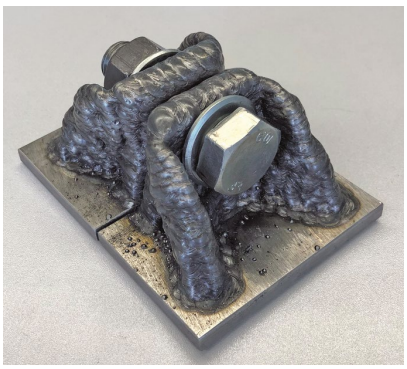

(b)

Figure. 11 (a) 3D printed stiffener, (b) 3D printed optimised connection

To take full advantage of the geometry flexibility of 3D printed components, structural optimisation methodology is involved during the establishment and optimisation of 3D models. Structural optimisation has three common categories, sizing optimisation, shape optimisation, and topology optimisation.

For sizing optimisation, the design variables of structural members, such as cross-section size and plate thickness, are optimised (Feucht, Lange & Erven, 2019). When all structural members use profile steel, some members under compression loading will be assigned with larger cross-sections to decrease the member slenderness. Other members under tensile loading, will be assigned with smaller cross-sections to increase the member slenderness. Hence, the differences among the maximum absolute magnitude of stresses in different structural members can be diminished, minimising the total structural weight.

For shape optimisation, the shape of the design domain is optimised (Bendsøe & Sigmund, 2004). This optimisation can minimise the maximum stress within the design domain to mitigate the adverse effect caused by stress concentration. Hence, the structural material can be saved, reducing the total structural weight. However, shape optimisation cannot remove the material at a position where the magnitude of stresses is lower than that of the surrounding material. To delete such 'useless' material from the design domain, topology optimisation is developed.

Topology optimisation is a mathematical method to optimise material distribution in the design domain according to the given load conditions, constraints, and performance indicators, (Bendsøe & Sigmund, 2004). The performance indicators can be the reduction of the design domain volume without a significant decrease in structural strength. By drilling holes at the unstressed position, the geometry of the design domain is more intricate, which makes the design domain too complex to be fabricated by subtractive manufacturing. WAAM or other AM methods is capable enough to handle such complex geometry (Figure. 12). Hence, AM is a 'good partner' of topology optimisation. This optimisation together with AM has a bright application prospect in the construction, automotive industry, and aerospace industry, becoming a research focus. One of the research directions is to assess the structural behaviour of optimised components, for example, the relationship between load-bearing capacity for T-stub endplates and volume of design domain (Figure. 13) (Buchanan & Gardner, 2019; Feucht, Lange & Erven, 2019; Hayley, 2017).

Figure. 12 Flexible geometry of the topology-optimised AM nodes (Galjaard et al., 2015)

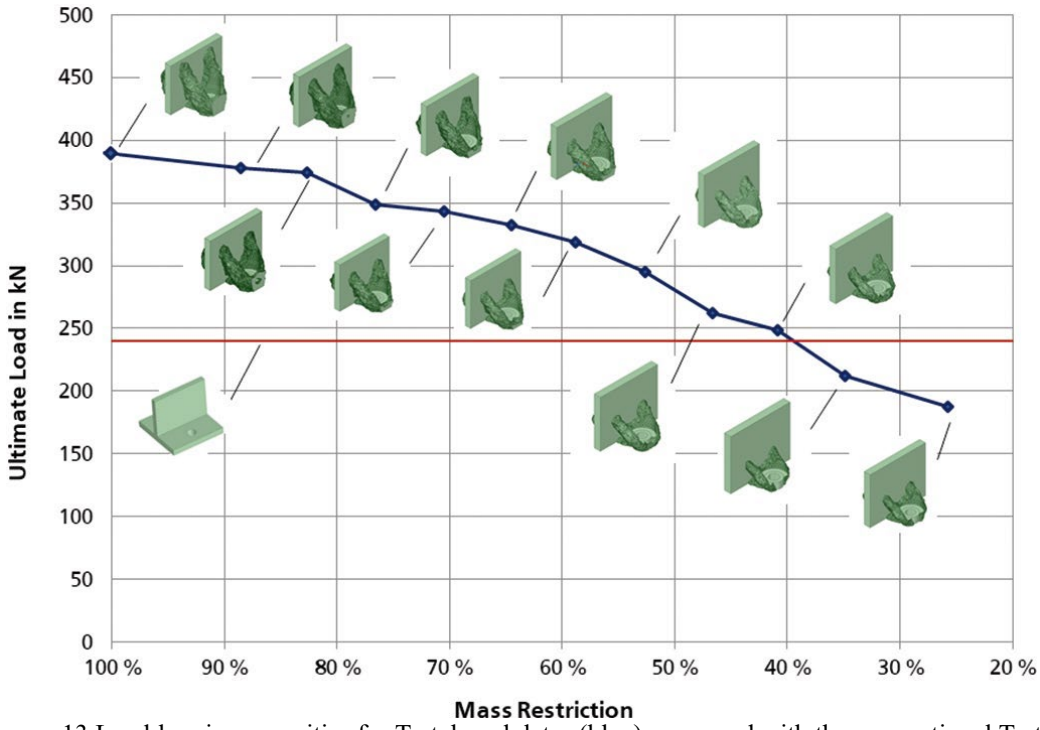

Figure. 13 Load-bearing capacities for T-stub endplates (blue) compared with the conventional T-stub endplates (red) (Feucht, Lange & Erven, 2019)

Following the flow chart (Figure. 14), in the following sections, the influence factors of topology-optimisation results and the structural performance of topology-optimised beam-to-column joints are explored.

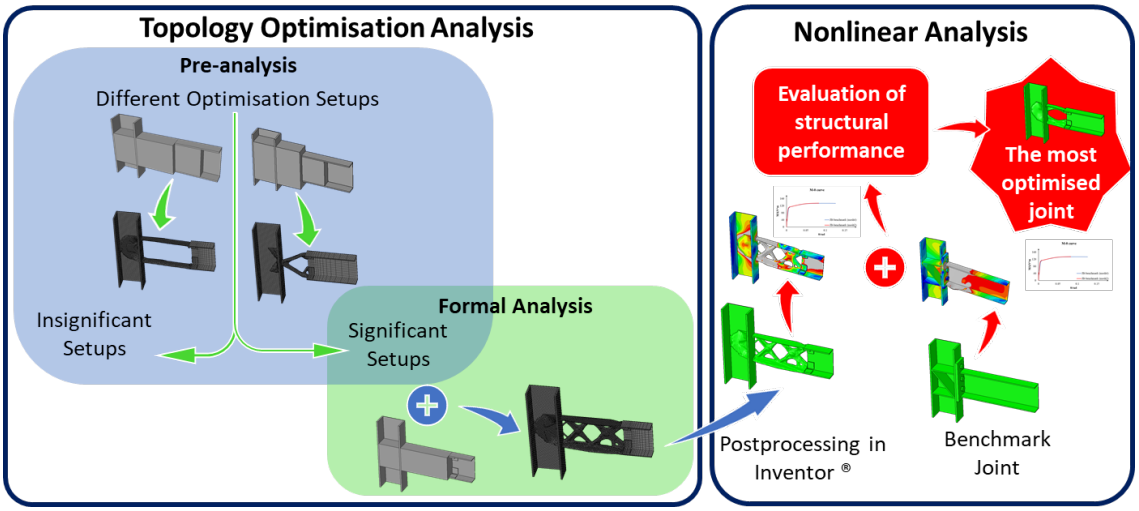

Figure. 14 The flow chart of this research project

2. TOPOLOGY OPTIMISATION OF BEAM-TO-COLUMN JOINTS

This section aims to describe topology optimisation models and the optimised results and discuss the influence factors.

2.1. Definition of optimisation task

The cross-section sizes of columns and beams are UC203x203x46 and UB203x133x25 (Figure. 15), respectively, which are preliminary selections and based on prior experience. The beam-to-column joints (Figure. 16), subjected to optimise, locate at the 1st and 2nd floor level of a steel moment frame. The design domains are coloured in green, blue and red (Figure. 16). The green domain refers to the stiffener inside the column, which has the same height as the blue domain. The blue domain refers to the connection part between columns and beams. With the help of the blue domain, the beam section stops at a position away from the column flange surface and no longer needs to resist a large hogging moment. The red domain refers to the connection part inserted into the beam, which should satisfy the requirement the bolt arrangement. Hence, the blue and red domains refer to the connection between beams and columns.

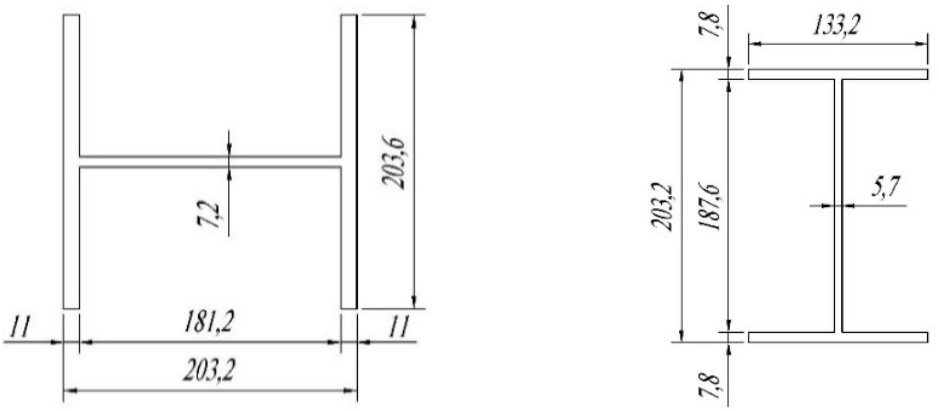

(a) UC203x203x46 (b) UB203x133x25

Figure. 15 Cross-section size of (a) columns and (b) beams

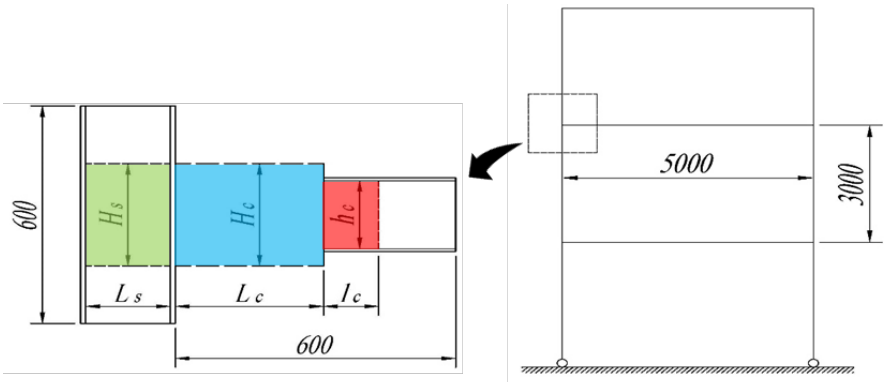

Figure. 16 Position of the beam-to-column joints and the general dimension of design domains

Within a moment frame, these beam-to-column joints should be able to sustain hogging moments. As the United Kingdom locates outside the seismic zone, non-seismic loading condition is considered for the topology optimisation. To simplify the topology optimisation task, the magnitude of external loads is calculated based on the moment resistance and shear force resistance of the beam section.

2.2. Description of FE models for topology optimisation

Topology optimisation was performed by Abaqus Topology Optimisation Module (ATOM). There are two topology optimisation analyses with different aims.

The first analysis aims to investigate influence factors on the topology-optimised results and to distinguish the significant factors and the insignificant factors. As the optimised stiffeners and connections are printed on the columns and connected with beams by bearing-type high-strength bolts, the arrangement of these bolts is predetermined through the first analysis as well. Hence, the first analysis is a pre-analysis. The results of this analysis are discussed in Section 2.3.1, 2.3.2, and 2.3.3.

The second analysis aims to optimise the design domains, with the consideration of the bolt arrangement. In Section 3 and 4, the structural performance of the optimised design domain is analysed and assessed by comparison with the benchmark joint. It should highlight that only the variation of the significant influence factors is considered in this analysis. Hence, the second analysis is formal analysis. The results of this analysis are discussed in Section 2.3.4, 2.3.5, 2.3.6, 2.3.7 and 2.3.8.

To simplify the optimisation analysis, linear topology optimisation is performed for both optimisation analyses. Hence, the linear material property is considered for all optimisation models. Elastic modulus and Poison's ratio are equal to 200GPa and 0.3, respectively. The analysis step is the static, linear perturbation.

Furthermore, simplified ½ models are established (Figure. 17 (b)) in both analyses. The information for optimisation models is described in the following paragraph:

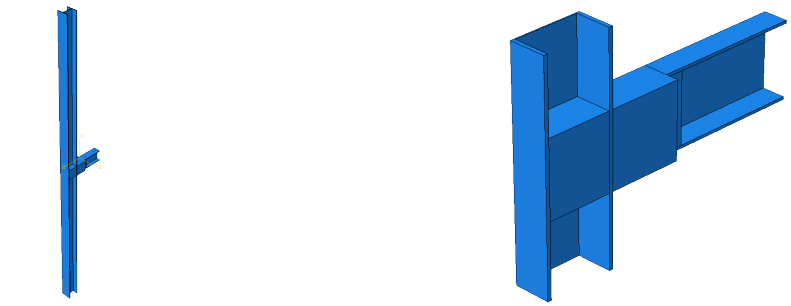

(a) Full model (b) Simplified ½ model

Figure. 17 Optimisation models in Abaqus

- **The length of column and beam in models**

Unlike the full models (Figure. 17 (a)), a small part of the column, which is 600mm long, is modelled in simplified models. Similarly, a small part of the beam is modelled. The beam length beam varies along with the change of the green domain length (L_c) among different models. But the distance between the beam end and the column flange is constant and equal to 600mm (Figure. 16).

- **Boundary condition**

Each end surface of the column is coupled with a point, 2700mm away from the column surface, to model a 6000mm long column (Figure. 18 (a)). Symmetry boundary condition is assigned to the symmetry surface (Figure. 18 (a)), which is the surfaces of models parallel to the yz-surface. All contact surfaces between two model parts are tied together.

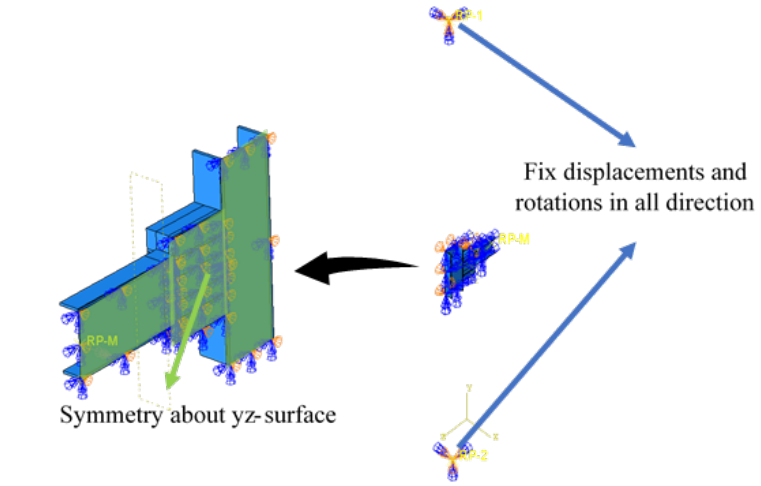

(a)

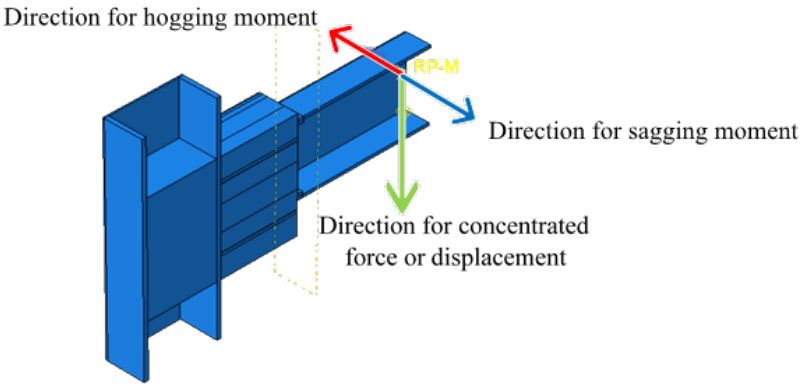

(b)

Figure. 18 (a) Boundary condition and (b) external loading position for the optimisation model in Abaqus

- **Loading cases**

As for external loads, these loads are applied at the central point of the beam end surface. And there are three loading cases in these optimisation analyses. For combined

moment and shear force case (MS), one concentrated downward force and one hogging moment are applied. For a pure shear force case (PS), one concentrated downward force and one sagging moment are applied. This sagging moment is used to counteract the hogging moment caused by this downward force. For a pure hogging moment case (PM), only one hogging moment is applied.

In pre-analysis, each model is assigned to a single loading case, while in formal analysis, each model is assigned to multiple loading cases. The definition of the loading case for each model is listed in Appendix B.

- **Mesh size and element type**

In pre-analysis, models have two different mesh sizes (4 and 8), while in formal analysis, the mesh size for all models remains unchanged and equal to 4, based on the results in Section 2.3.1.

Unlike the mesh size, C3D8R is used for all models in both analyses.

- **Design domain**

The definition of the design domain varies between these analyses. And the geometry of each design domain for all models is listed in Appendix B.

In pre-analysis, the green domain is assigned as an individual design domain, stiffener domain, while the blue and red domains are assigned as another individual design domain, connection domain. It should highlight that the stiffener domain will not appear in every model in this analysis.

In the formal analysis, the assignment of the stiffener domain remains unchanged, while the blue domain is assigned as the connection domain, based on the results in Section 2.3.3.

- **Optimisation target**

The ratio between the final and initial volume of the design domain, defined as optimisation constant, is assigned separately for the stiffener and connection domain. In pre-analysis, the optimisation target is to decrease this ratio to 10% in stiffener and connection domains. In formal analysis, this ratio (η_c and η_s) is calculated by Eq.1, Eq.2, Eq.3 and Eq.4. It should highlight that $V_c^{normalised}$ varies from 0.7, 1.0, to 1.3, while $V_s^{normalised}$ is equal to 1.0 for all models.

$$V_c^{normalised} = \frac{V_c^{optimised}}{L_c * A_{beam}} \quad \text{Eq. 1}$$

$$\eta_c = \frac{V_c^{optimised}}{V_c^{initial}} \quad \text{Eq. 2}$$

$$V_s^{normalised} = \frac{V_s^{optimised}}{V_s^{benchmark}} \quad \text{Eq. 3}$$

$$\eta_s = \frac{V_s^{optimised}}{V_s^{initial}} \quad \text{Eq. 4}$$

where,

$V_c^{normalised}$ and $V_s^{normalised}$ are the normalised volume of the optimised connection domain and the optimised stiffener domain, respectively.

$V_c^{optimised}$ and $V_s^{optimised}$ are the volume of the optimised connection domain and the optimised stiffener domain, respectively.

$V_c^{initial}$ and $V_s^{initial}$ are the initial volume of the connection domain and the stiffener domain, respectively.

$V_s^{benchmark}$ is the stiffener volume in the benchmark joint, which is equal to 372cm^3.

A_{beam} is the cross-section area of UB203x133x25, which is equal to 32 cm^2.

- **Objective function**

The objective function is to minimise the sum of strain energy in both stiffener and connection domains for both analyses.

- **Optimisation algorithm**

General optimisation is the selected optimisation algorithm for both analyses, which is the default setting in Abaqus.

- **Weights for loading cases**

The weights for loading cases are another important optimisation parameter. In pre-analysis, a single loading case is considered, so that the calculation of this weight is not involved. In formal analysis, these weights are calculated based on two main criteria, load control criterion and initial-strain-energy control criterion.

In the load control criterion (LC criterion), these weights are all equal to 1 since all loading cases are treated equally. Under this criterion, different external loading cases are treated equally, but their contributions to optimisation results are not treated equally.

These contributions can be reflected in the values of the initial strain energy, which is defined as the magnitude of strain energy in the design domain with unoptimised geometry under different loading cases. Form Table. 1, these values are influenced by loading cases and the height to length ratio (H_c/L_c) of the blue domain. Since the strain energy is the focus of the objective function, such differences in this energy need to be considered. Hence, the SE and SEA criterion are defined.

Table. 1 Initial strain energy of different design domains under different loading conditions

H_c/L_c	Loading Condition	Green Domain	Blue Domain	Blue domain / Green domain
0.5	MS	15327	42802	2.79
	PS	15346	37772	2.46
	PM	6972	20212	2.90
1	MS	192	56503	293.98
	PS	192	13236	69.02
	PM	248	11443	46.13
1.5	MS	26084	143855	5.52
	PS	26118	87050	3.33
	PM	11918	50880	4.27

In the initial-strain-energy control criterion, there are two sub-criterions, SE and SEA criterion. In these sub-criterions, these weights are calculated according to initial strain energy. In the SE criterion, these weights (Table. 2) can ensure that the sum of the weighted initial strain energy in the stiffener and connection domain remains constant under different loading cases. Even this sum is constant for different loading cases, but the initial strain energy in green and blue domains still varies in these loading cases, which means the contribution of different domains in certain loading cases is different.

Table. 2 Calculated weights for the initial-strain-energy control criterion (the SE and SEA criterion)

H_c/L_c	Loading Case	SE Criterion	SEA Criterion	
			Green Domain	Blue Domain
0.5	MS	0.42241	0.00615	0.2433
	PS	0.4331	0.49024	0.1843
	PM	0.14449	0.00361	0.07239
1	MS	0.18432	0.00613	0.11661
	PS	0.72917	0.49027	0.33279
	PM	0.08651	0.0036	0.0506
1.5	MS	0.26609	0.01684	0.15805
	PS	0.61873	0.47331	0.27917
	PM	0.11518	0.00985	0.06278

To make this difference into account, in the SEA criterion, these weights (Table. 2) are redetermined to ensure that the weighted initial strain energy under different loading cases remains constant in each design domain.

2.3. Topology optimisation results

The optimisation results are presented in the following section. Relevant influence factors are described as well. The model's name consists of three segments that have

different meanings in pre-analysis and formal analysis. The naming system is described in Appendix A.

2.3.1. Effect of stiffeners

The effect of the stiffener is explored under two loading conditions, pure shear force (PS) and combined hogging moment and shear force (MS). In both loading conditions, the stiffener only affects the optimised geometry of the blue domain, located between beam and column, slightly (Figure. 19). Some unique geometry occurs in the blue domain in P-0738PS-SDM4 and P-0738MS-SNM4, compared with the other two models under the same loading condition. But compared with its surrounding structure, this geometry has a large slenderness ratio (Figure. 19) and cannot have a significant contribution to the resistance of optimised beam-to-column joint. Hence, this unique geometry is neglectable.

Thus, the strengthened status of the column is an insignificant influence factor. In formal analysis, the stiffener (green domain) and the connection (blue domain) are optimised together.

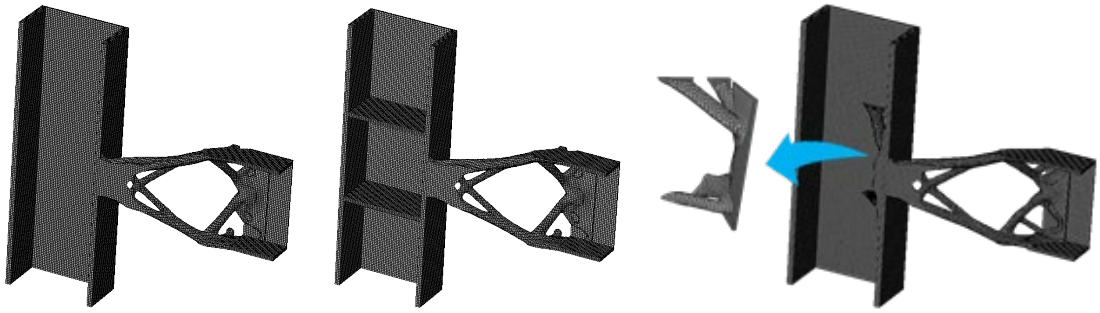

1) P-0738PS -SNM4 2) P-0738PS-SGM4 3) P-0738PS-SDM4

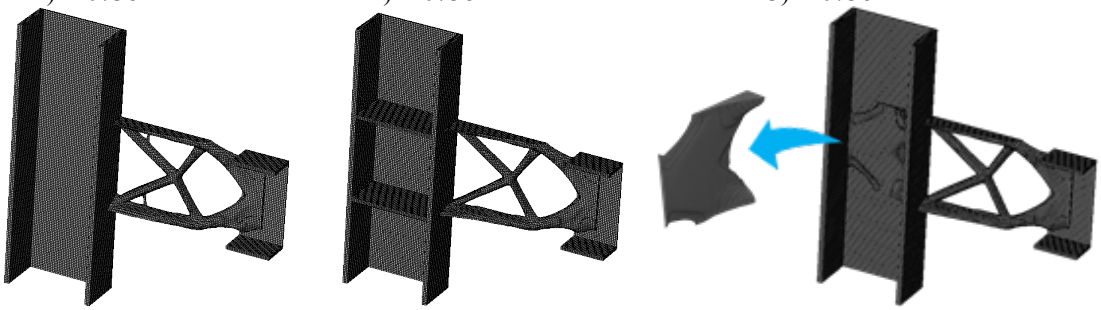

4) P-0738MS -SNM4 5) P-0738MS-SGM4 6) P-0738MS-SDM4

Figure. 19 Optimisation results used to investigate the effect of stiffeners

2.3.2. Effect of the mesh size

Theoretically, the smaller the mesh size is, the more complex geometry the optimised results can have, better loading performance these results can have. This is because models with finer mesh can have a smoother stress distribution, through computation. And the more unstressed material can be found out and deleted by topology optimisation. But considering the numerous computing hours caused by such tiny mesh in models, models with mesh size equalling to 4 are the models with the finest mesh in

pre-analysis.

The results, with different geometry of blue domain but under the same loading condition, are displayed in Figure. 20. These results prove the conclusion in the last paragraph that the effect of mesh size is significant. Thus, in formal analysis, models with a mesh size equal to 4 are optimised.

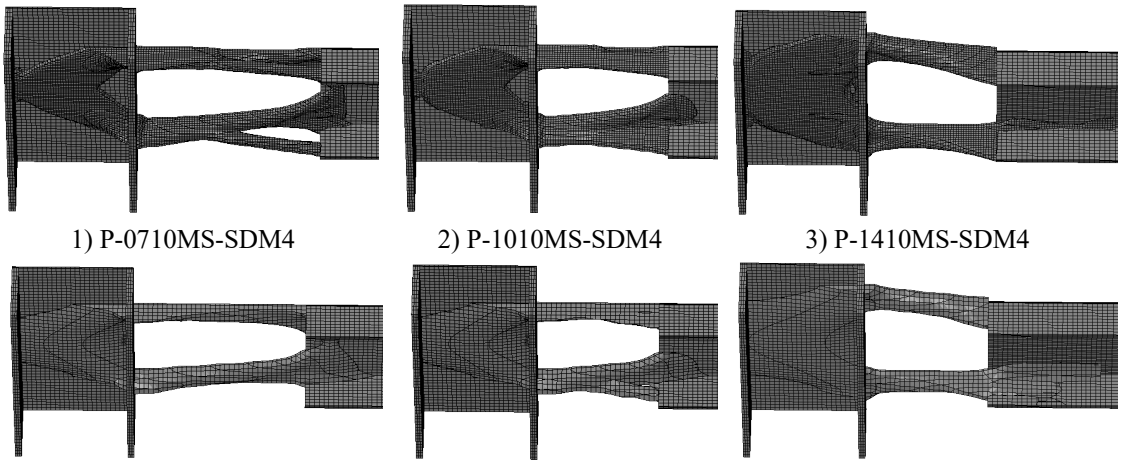

1) P-0710MS-SDM4 2) P-1010MS-SDM4 3) P-1410MS-SDM4

4) P-0710MS-SDM8 5) P-1010MS-SDM8 6) P-1410MS-SDM8

Figure. 20 Optimisation results used to investigate the effect of mesh size

2.3.3. Effect of the red domain length (l_c)

The results, with different lengths (l_c) of the red domain but under the same loading condition, are displayed in Figure. 21. Obviously, this length (l_c) impacts the optimised geometry of the blue domain slightly. It is because topology optimisation should be able to make full use of the existing part of the model, besides optimising the best distribution of material. If the optimised geometry extends into the beam too much, the connection domain will start to sustain loading at the position that is far away from the beam end. Once the connection domain is stressed, the beam section no longer sustains loads individually, which indicates the material of the beam is not utilised fully. Hence, no matter how long this length (l_c) is, the topology optimisation should return a result, having only a small portion of the material inside the beam.

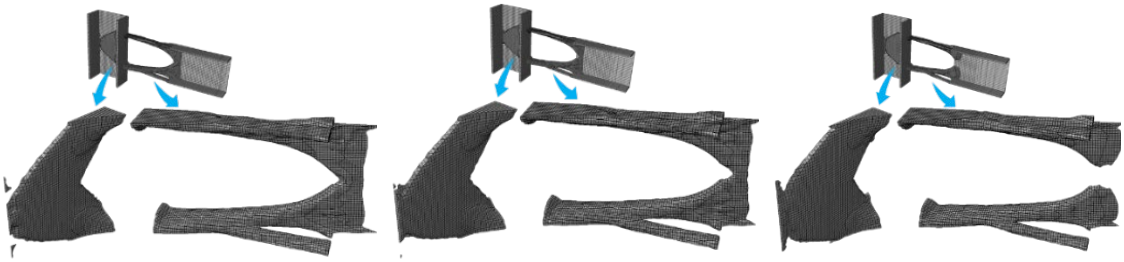

1) P-0707MS-SDM4 2) P-0710MS-SDM4 3) P-0714MS-SDM4

Figure. 21 Optimisation results used to investigate the effect of l_c

However, if this length is too small, the load propagation path may be affected, which will affect the stress distribution. The impact caused by the change of stress

distribution is mainly concentrated in the red domain itself and will not lead to an excessive change in the geometry of the blue domain, which can be observed in P-0714MS-SDM4 in Figure. 21.

Thus, the effect of the red domain length (l_c) can be neglected, as the geometry of the blue domain is the focus of this dissertation.

2.3.4. Effect of loading cases

The comparison among the results under single loading conditions and multiple loading conditions (Figure. 22) highlights the advantage of models optimised under multiple loading conditions and the effect of loading cases. It is because if a beam-to-column joint is optimised under a single loading case, the result may be likely to have poor performance under other loading cases. For example, the result of FJ-1007PS-N (Figure. 22) has low bending moment resistance and is not the desired result.

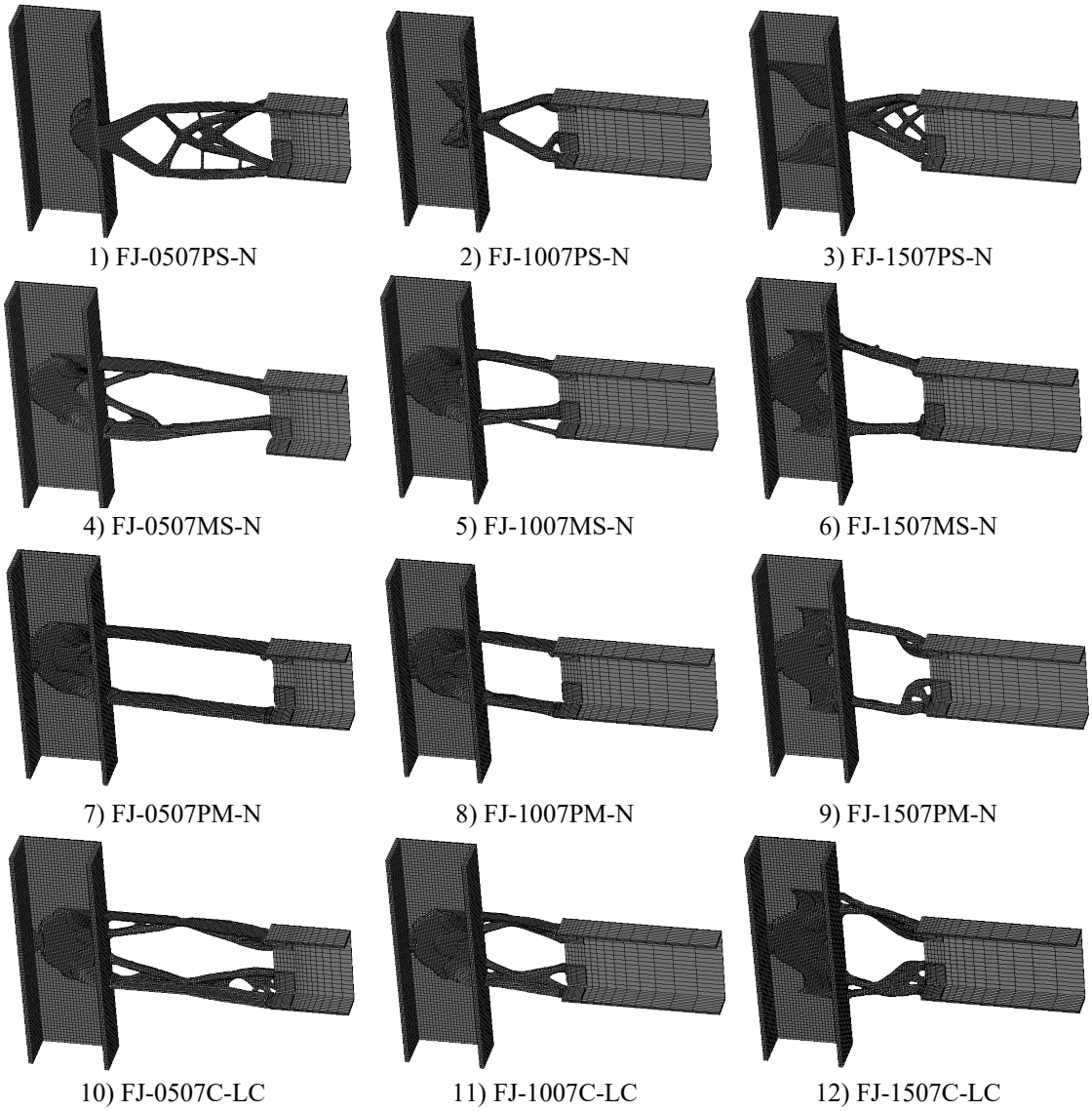

Figure. 22 Optimisation results used to investigate the effect of loading cases

On the other hand, a joint optimised under multiple loading cases may have poor performance under certain loading conditions, compared with the result optimised under that loading case, but is more likely to have an even performance under different loading cases. Since, in the real building, structures are unlikely to be under a single loading case during its service life, beam-to-column joints under multiple loading cases are more realistic.

Thus, the effect of the loading case is significant. In formal analysis, beam-to-column joints are optimised under multiple loading conditions.

2.3.5. Effect of the blue domain length (L_c)

By comparing the six results in the first two rows of Figure. 23, it is easy to conclude that the effect of blue domain length is significant. The optimised geometry changes with the variation of blue domain length, because of the change in the stress distribution. Meanwhile, without the nonlinear analysis results of these joints, it is difficult to select the best-optimised geometry.

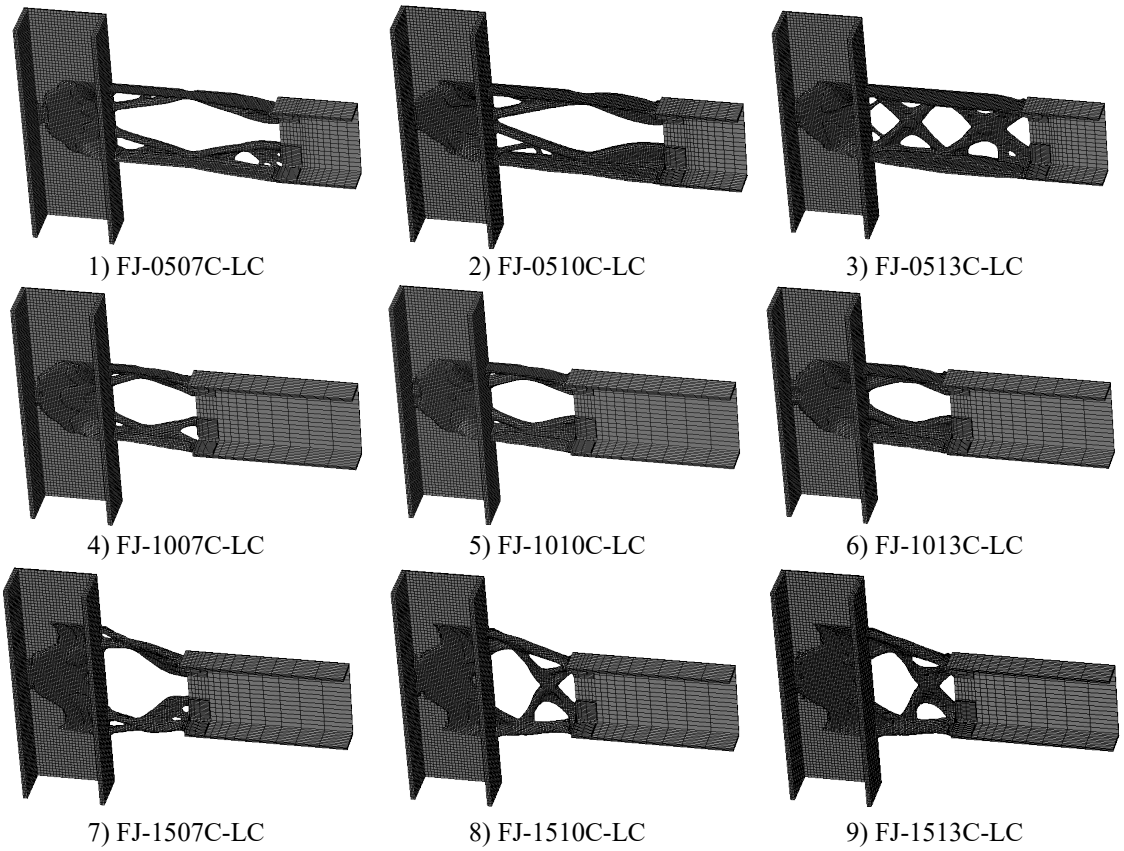

1) FJ-0507C-LC 2) FJ-0510C-LC 3) FJ-0513C-LC

4) FJ-1007C-LC 5) FJ-1010C-LC 6) FJ-1013C-LC

7) FJ-1507C-LC 8) FJ-1510C-LC 9) FJ-1513C-LC

Figure. 23 Optimisation results used to investigate the effect of L_c, H_c and η_c

2.3.6. Effect of the blue domain height (H_c)

Similarly, the six results in the last two rows of Figure. 23 indicates that the effect of the blue domain height is significant. Due to the same reason as Section 2.3.5, the difference in the optimised geometry is notable.

Thus, it is an effective strategy to enrich the form of the optimised geometry by changing the geometry of the focused design domain, which is the blue domain in this dissertation. Nonlinear analysis should be conducted to estimate the structural performance of the geometry, to find the desired geometry.

2.3.7. Effect of the optimisation target (η_c)

The results, in a row family but different columns of Figure. 23, indicate that the blue domain height is another significant influence factor. It is not because of stress distribution, but because of the optimisation target, the volume of the optimised geometry. This volume is connected to how much material should be deleted, which causes the variation in the optimised geometry. Another reason is that some geometry may require at least a certain amount of material to form, for example, the truss-type geometry in FJ-0513C-LC (Figure. 23).

Consequently, it is another effective strategy to enrich the form of optimised geometry by changing the optimisation target, which is the volume of optimised geometry in this dissertation.

2.3.8. Effect of weights for loading conditions

The results in a row family but different columns of Figure. 24 indicate that the effect of weights for loading cases should be considered. According to the definition of the objective function, the weighted strain energy is the accordance for Abaqus to find the unstressed material. The importance of loading conditions is reflected by these weights. The calculation of these weights is based on the consideration of criteria, which is affected by the objective function.

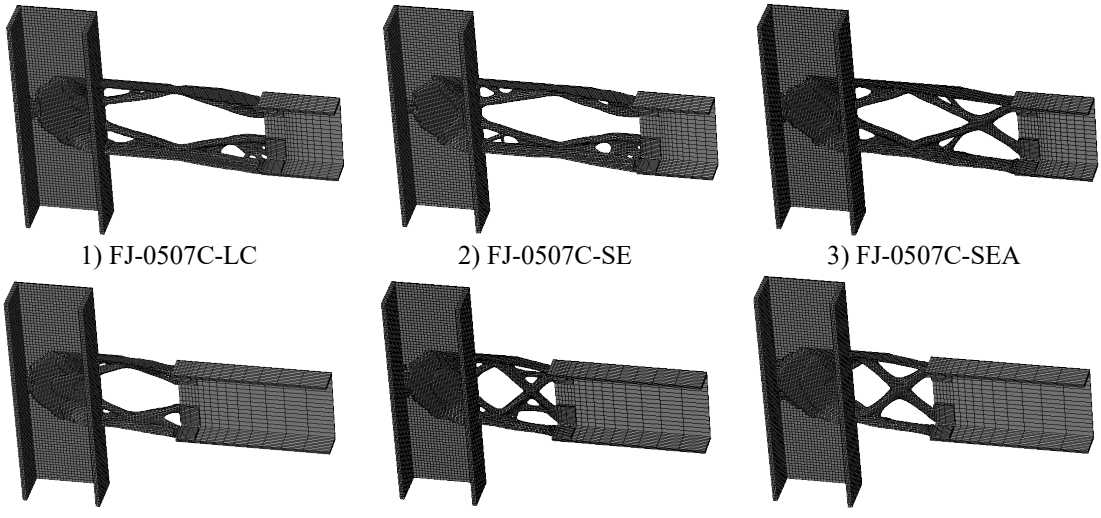

1) FJ-0507C-LC 2) FJ-0507C-SE 3) FJ-0507C-SEA

4) FJ-1007C-LC 5) FJ-1007C-SE 6) FJ-1007C-SEA

Figure. 24 Optimisation results used to investigate the effect of weight for loading cases

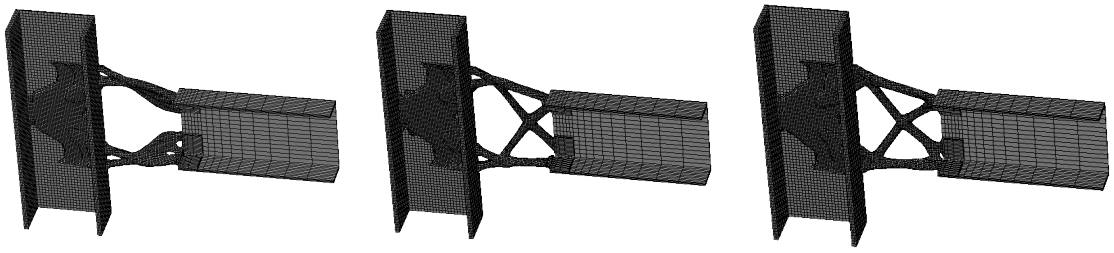

7) FJ-1507C-LC 8) FJ-1507C-SE 9) FJ-1507C-SEA

Figure. 24 Optimisation results used to investigate the effect of weight for loading cases (continuous)

Thus, it is effective to use different weights to enrich the form of optimised geometry. To wisely use these weights, during the determination of these weights, the actual loading condition of beam-to-column joints and the selection of the objective function are supposed to be considered.

In this dissertation, one important criterion is to treat all loading conditions equally, which may not be in accord with the actual situation. Hence, the methodology to calculate these weights is one of the focuses in future research projects.

3. NONLINEAR ANALYSIS OF BENCHMARK AND OPTIMISED JOINTS

In this section, the model for the benchmark beam-to-column joint is established and analysed in Abaqus. The optimised joints in formal analysis are also analysed.

3.1. Selection of benchmark joints

The benchmark beam-to-column joint is used to estimate the performance of optimisation results so that the selection of this joint should be in accord with the practical case in construction. Hence, according to the recommendation (Figure. 25) in *Joints in Steel Construction: Moment-Resisting Joints to Eurocode3* (Brown & Lles, 2013), the benchmark joint is decided as an end-plate beam-to-column joint (Figure. 26). High-strength bearing-type bolts are adopted in this joint.

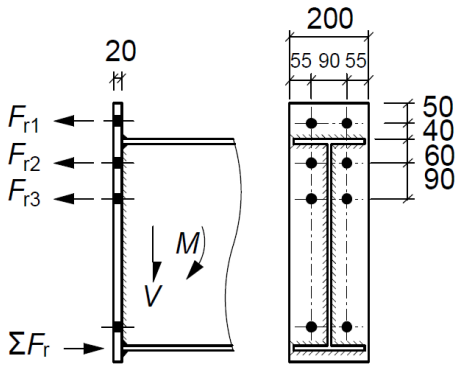

Figure. 25 Bolt arrangement recommendation for beam sizes 457 UKB and below (Brown & Lles, 2013)

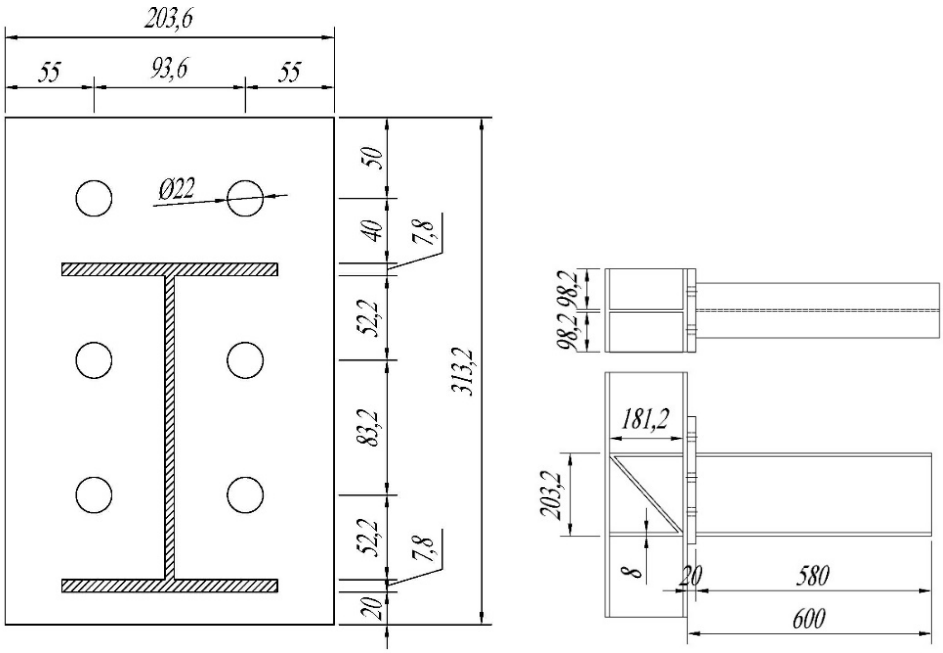

Figure. 26 Dimension of the benchmark joint

3.2. Postprocessing of optimised joints

The optimised design domains often have minor defects. For example, the

extremely slender legs (Figure. 27) are unqualified to sustain external loads, but a considerable number of elements are used to mesh these legs. Hence, to reduce these unnecessary elements, the postprocessing of these domains is indispensable.

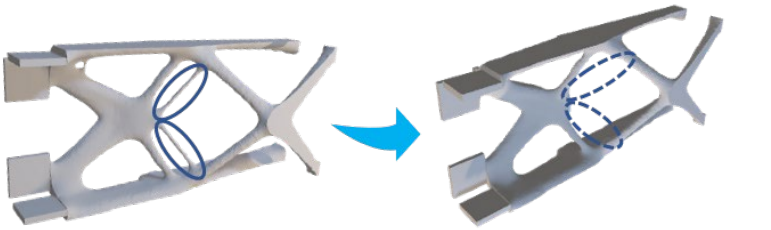

Figure. 27 Example for the defective domain and the processed domain

During the postprocessing, these defective domains are exported from Abaqus and imported into software, Inventor, in which these defects are modified or deleted. These processed domains are re-imported into Abaqus to establish the nonlinear analysis models.

All the processed design domains are displayed in Figure. 28.

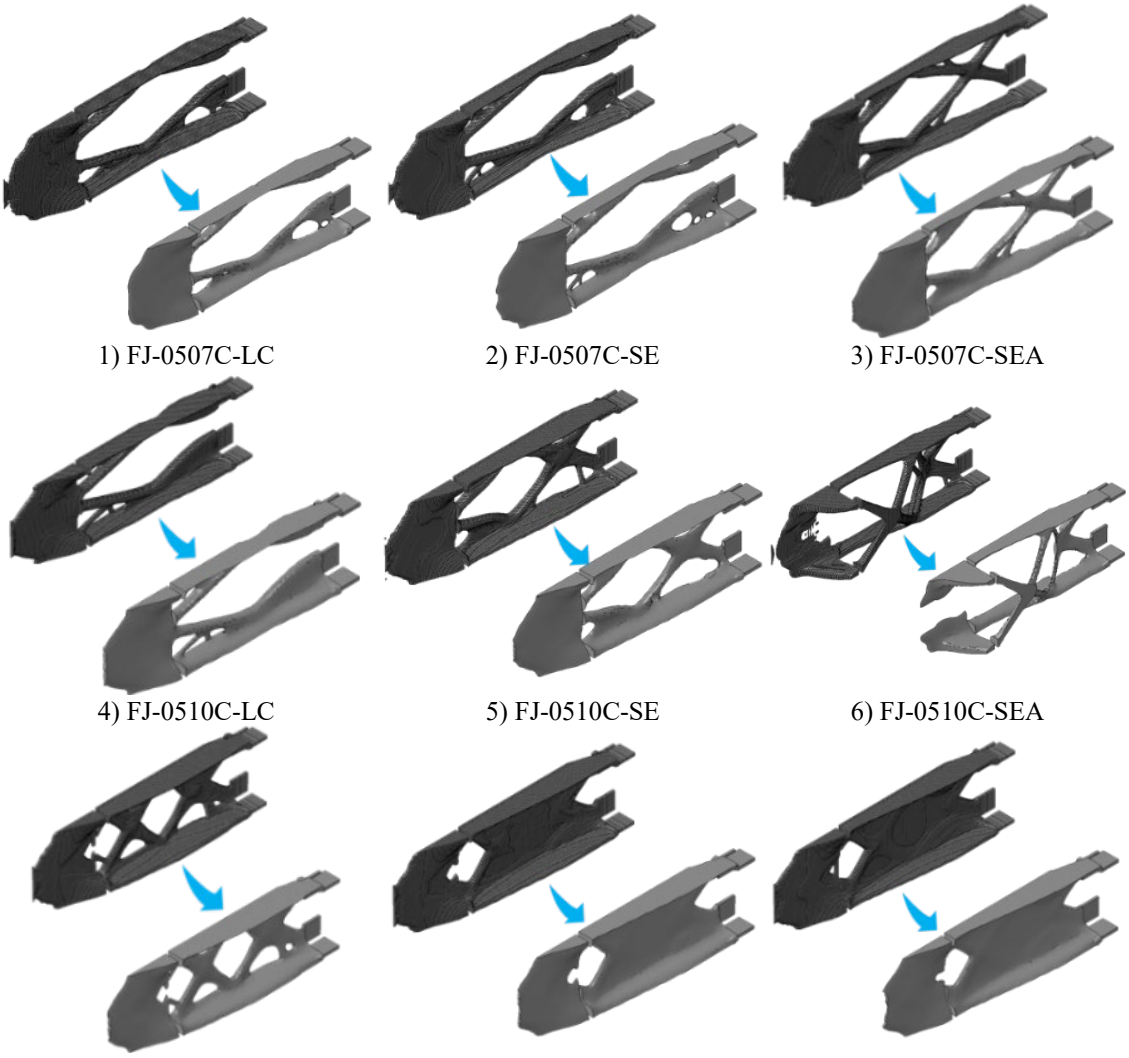

Figure. 28 The defective domain (top-left) and the processed domain (bottom-right) for all nonlinear analysis models

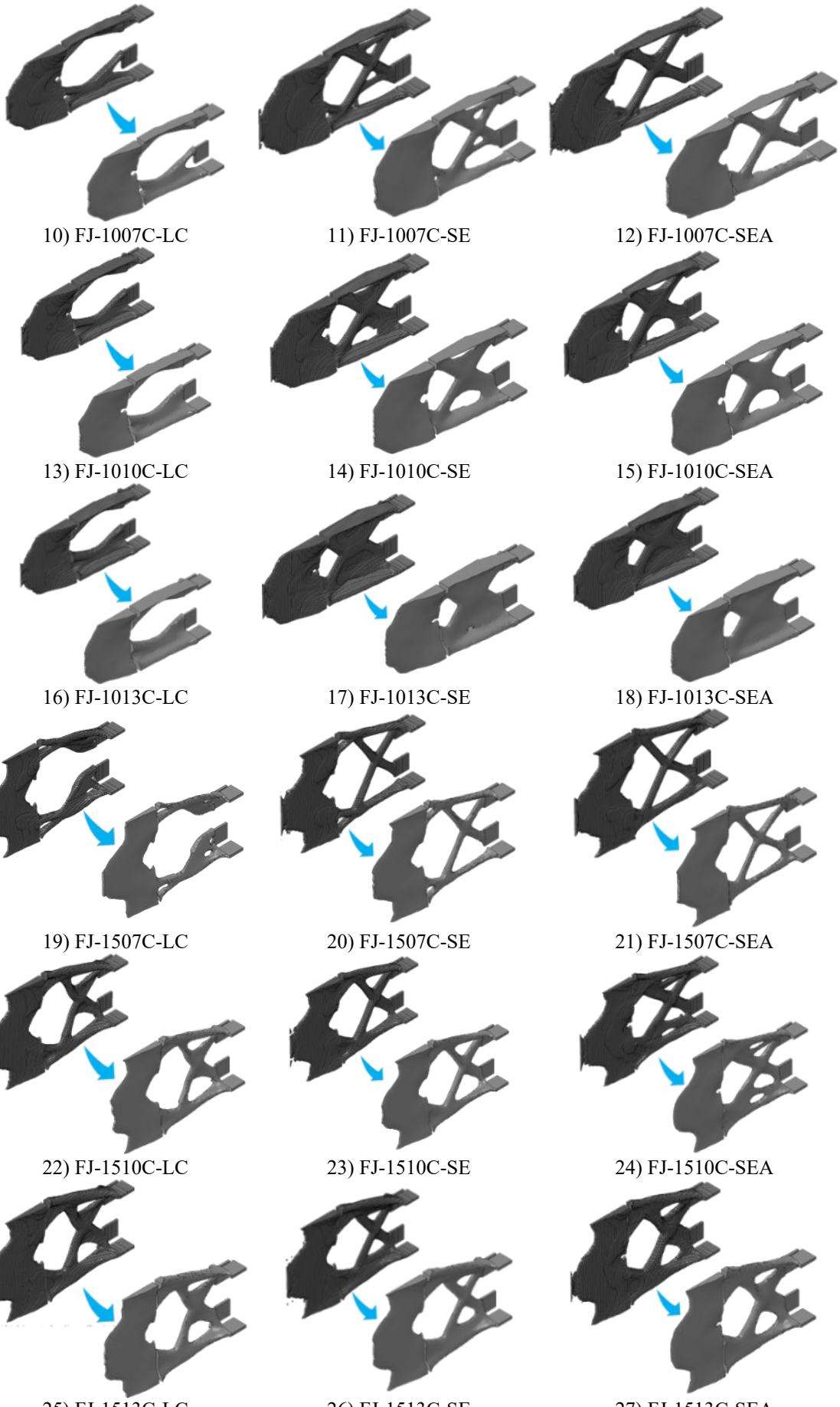

10) FJ-1007C-LC 11) FJ-1007C-SE 12) FJ-1007C-SEA

13) FJ-1010C-LC 14) FJ-1010C-SE 15) FJ-1010C-SEA

16) FJ-1013C-LC 17) FJ-1013C-SE 18) FJ-1013C-SEA

19) FJ-1507C-LC 20) FJ-1507C-SE 21) FJ-1507C-SEA

22) FJ-1510C-LC 23) FJ-1510C-SE 24) FJ-1510C-SEA

25) FJ-1513C-LC 26) FJ-1513C-SE 27) FJ-1513C-SEA

Figure. 28 The defective domain (top-left) and the processed domain (bottom-right) for all nonlinear analysis models (continous)

3.3. Description of FE models

3.3.1. FE models for benchmark joints

The benchmark model, named JB-benchmark (Figure. 29), is established based on the geometry in Figure. 26. The key analysis setups of this model are listed below.

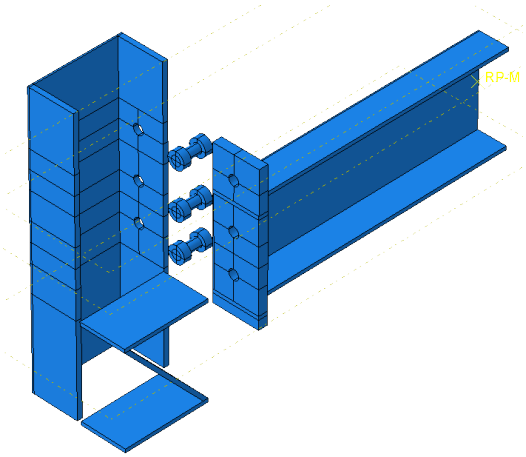

Figure. 29 Each part of the benchmark beam-to-column joint model

- **The material constitutive models**

The steel grade for the column, beam and stiffener is S355, while the grade for high-strength bolts is Grade 8.8. The material constitutive model of S355 is the quad-linear stress-strain curve (Figure. 30(a)) proposed by (Yun & Gardner, 2017), which is defined by three basic material property valuables (E, f_y and f_u) and by five formulas (Eq. 5 to Eq. 9). For the less important model part, bolts, the material constitutive model is the elastic, hardening model (Figure. 30(b)) (Yun & Gardner, 2017).

$$f(\varepsilon)=\begin{cases} E\varepsilon \text{ for } \varepsilon \le \varepsilon_y \\ f_y \text{ for } \varepsilon_y < \varepsilon \le \varepsilon_{sh} \\ f_y + E_{sh}(\varepsilon-\varepsilon_{sh}) \text{ for } \varepsilon_{sh} < \varepsilon \le c_1\varepsilon_u \\ f_{c_1\varepsilon_u} + \frac{f_u - f_{c_1\varepsilon_u}}{\varepsilon_u - c_1\varepsilon_u}(\varepsilon - c_1\varepsilon_u) \text{ for } c_1\varepsilon_u < \varepsilon \le \varepsilon_u \end{cases} \quad \text{Eq. 5}$$

$$\varepsilon_u = 0.6\left(1-\frac{f_y}{f_u}\right) \text{ and } \varepsilon_u \ge 0.06 \text{ for hot-rolled steels} \quad \text{Eq. 6}$$

$$\varepsilon_{sh} = 0.1\frac{f_y}{f_u} - 0.055 \text{ and } 0.015 \le \varepsilon_{sh} \le 0.03 \quad \text{Eq. 7}$$

$$c_1 = \frac{\varepsilon_{sh} + 0.25(\varepsilon_u - \varepsilon_{sh})}{\varepsilon_u} \quad \text{Eq. 8}$$

$$E_{sh} = \frac{f_u - f_y}{0.4(\varepsilon_u - \varepsilon_{sh})} \quad \text{Eq. 9}$$

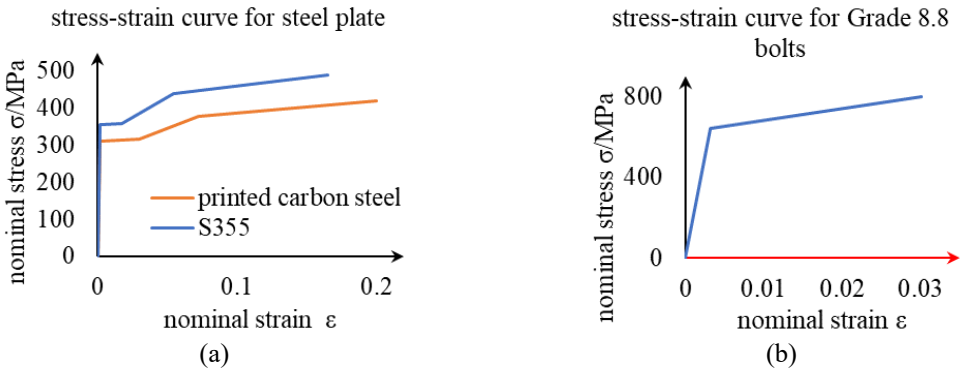

Figure. 30 The material constitutive models used in nonlinear analysis

- **Mesh size and element type**

JB-benchmark has two mesh sizes, 2 and 4. The result from the finer meshed model is used to assess the accuracy of the coarse meshed model, qualitatively.

C3D8R is a low-order element type with hourglassing in bending, marking it unsuitable to be used in bending dominant regions, such as the bolt and beam parts, so that C3D8R is used in the column and stiffener parts. C3D20R is a high-order element type without hourglassing in bending, used in bolt and beam parts.

- **Boundary conditions**

Since the benchmark models are the simplified ½ models, the setups of boundary conditions are similar to the FE models for topology optimisation.

Each end surface of the column is coupled with a point, 2700mm away from the column surface. The symmetry property is assigned to the symmetry surface.

The contact surfaces between column and stiffener are tied together. The friction coefficient for the contact surfaces between endplate and column equals 0.01.

To slightly prestress the bolts, both sides of the bolt head are loaded with a 10Pa pressure. Although this small amount of pressure cannot affect the mechanical performance of bearing-type bolts, it is indispensable and can help the model converge during the analysis.

- **Loading processing**

Unlike the optimisation FE models, which are force controlled, the nonlinear analysis models are loaded by a downward displacement applied at the centre of the beam end surface.

3.3.2. FE models for optimised joints

The nonlinear analysis models of optimised joints derive from the FE models, used in topology optimisation, by replacing the design domains with the post-processed optimised results.

The key analysis setups of these models are listed below.

- **The material constitutive models**

The steel grade for the column and beam is S355, while the material property of the optimised stiffener and connection is defined based on the printed carbon steel. The quad-linear stress-strain curve (Figure. 30(a)), proposed by (Yun & Gardner, 2017), is used as the material constitutive model for both types of material. But for the printed carbon steel, instead of calculating by Eq. 6 and Eq. 7, nominal values of the ultimate strain (ε_u) and strain-hardening strain (ε_{sh}) equal 0.3 and 0.02, respectively.

- **Mesh size and element type**

The mesh size and element type of column and beam parts remain unchanged, while the mesh size of the optimised stiffener and connection equals 4, while the element type is C3D10M.

- **Boundary conditions**

The nonlinear analysis models are consistent in the boundary condition setups with the optimisation models.

- **Loading processing**

Like the benchmark models, the nonlinear analysis models are loaded by a downward displacement, which is applied at the centre of the beam end surface.

4. COMPARISONS BETWEEN BENCHMARK AND OPTIMISED JOINTS

In this section, the performance of optimised joints is assessed. On the other hand, the effects caused by four factors, the calculation methodology of loading case weights, the length (L_c), height (H_c) and volume of the connection domain are discussed. This performance assessment includes the comparison of the selected variables between the optimised joints and the benchmark joints. These variables are the rotational stiffness (S), bending moment (M_y) and rotation angle (θ_y) at yield point, bending moment capacity (M_u) and rotational capacity (θ_u). The definitions of these variables are presented as follows.

- **The rotational stiffness (S)**

The initial stiffness is the tangent stiffness of the moment-rotation curve before the moment reaches the yield point (M_y). To obtain this curve, according to the proposed methodology in (Zhu et al., 2019), the connection rotation angle is calculated by Eq. 10, while the moment is calculated by Eq. 13.

$$\theta=\theta_t\text{-}arctan\left(\frac{PL^2}{3EI}\right)\text{-}\frac{\delta_2\text{-}\delta_3}{2h_b} \quad \text{Eq. 10}$$

$$P=2P_0*cos(\theta_t) \quad \text{Eq. 11}$$

$$\theta_t=\frac{\delta_1}{L} \quad \text{Eq. 12}$$

$$M=PL \quad \text{Eq. 13}$$

where,

P_0 is the recorded reaction force at Loading Point (Figure. 31).

L is the distance between the loading point and the column centre line, which equals 701.6mm.

I is the second moment of the beam cross-section, which equals 2340cm^4.

h_b is the beam height, which equals 203.2mm.

δ_1 is the recorded displacement in the y-direction at Loading Point (Figure. 31).

δ_2 and δ_3 are the recorded displacements in the x-direction at Point A and Point B (Figure. 31), respectively.

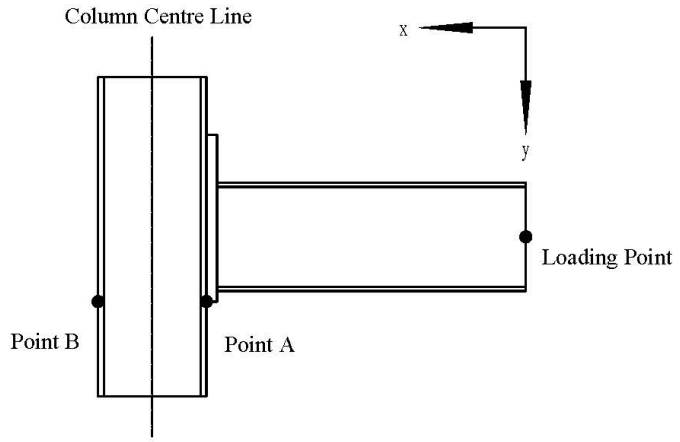

(a) Benchmark joints

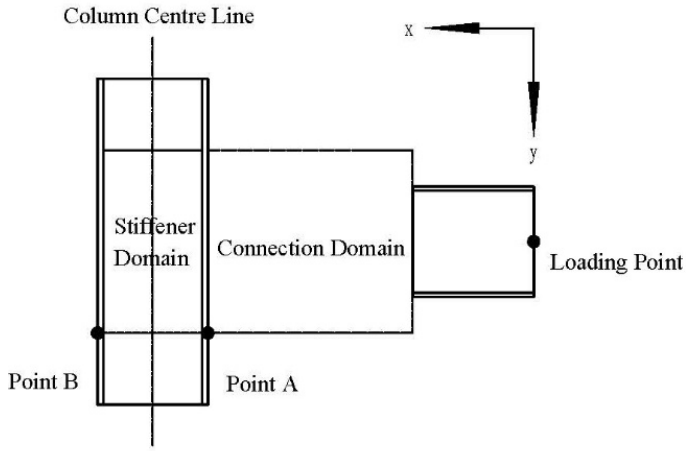

(b) Optimised joints

Figure. 31 Location of data collection points

For benchmark joints, the beam will slip under a slight external disturbance, because of clearance between the bolt shank and bolt hole and the small friction force between the contact surfaces of the endplate and the column. Hence, part of this curve of benchmark joints cannot be used to obtain the initial stiffness.

- **The bending moment (M_y) and rotation angle (θ_y) at yield point**

The yield point is defined as a point on the moment-rotation curve, where the tangent stiffness changes remarkably. The values of x- and y-coordinate of this point are θ_y and M_y, respectively.

- **The bending moment capacity (M_u) and rotational capacity (θ_u)**

The values of x- and y-coordinate of the top point of the moment-rotation curve are θ_u and M_u, respectively.

4.1. Nonlinear analysis result of benchmark models

Two models with different mesh sizes are analysis in Abaqus. The benchmark joint fails due to the local buckling of the compressed beam flange (Figure. 34). The

deformation of the column is considerably small compared with the beam, which meets the requirement of the 'strong column and weak beam'. Meanwhile, based on the results in Table. 3, the benchmark joint can be classified as a semi-rigid, full-strength joint.

On the other hand, the almost overlapping moment-rotation curves (Figure. 32), the identical failure models (Figure. 34) and the similar values of the selected performance variables (Table. 3) all indicate that the model with coarse mesh size is capable enough to provide accurate results. The accuracy of this model is further proofed by the energy-time curve (Figure. 33) because compared with the internal energy of models, all the other types of energy are considerably small. Hence, this coarse-meshed model is used as the benchmark model to assess the structural performance of the optimised joints in Section 4.2, since the model has the same mesh size as the FE models of the optimised joints.

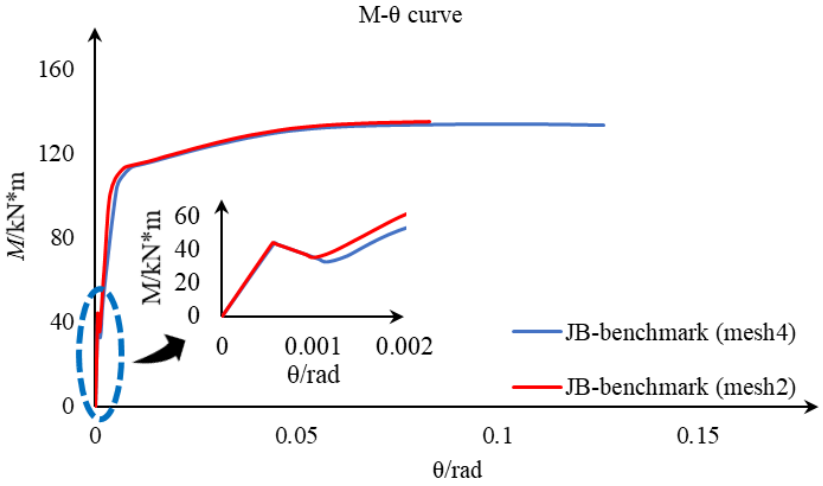

Figure. 32 Moment-rotation curves for benchmark joints

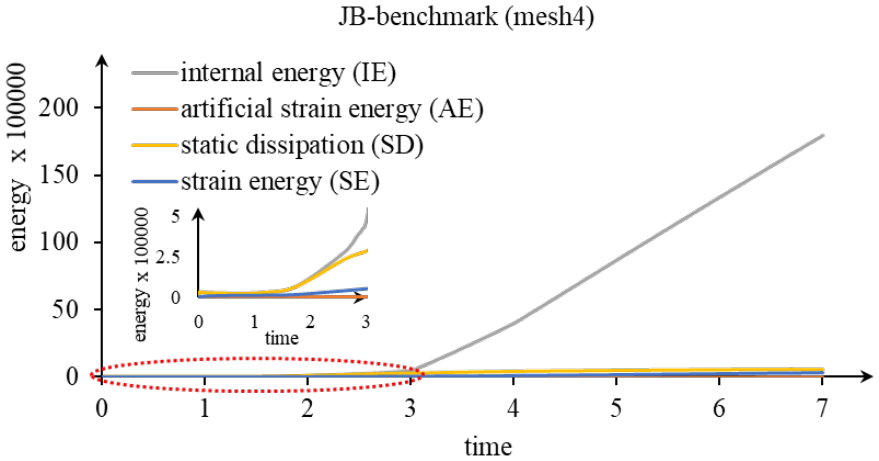

Figure. 33 Energy-time curve for benchmark joints

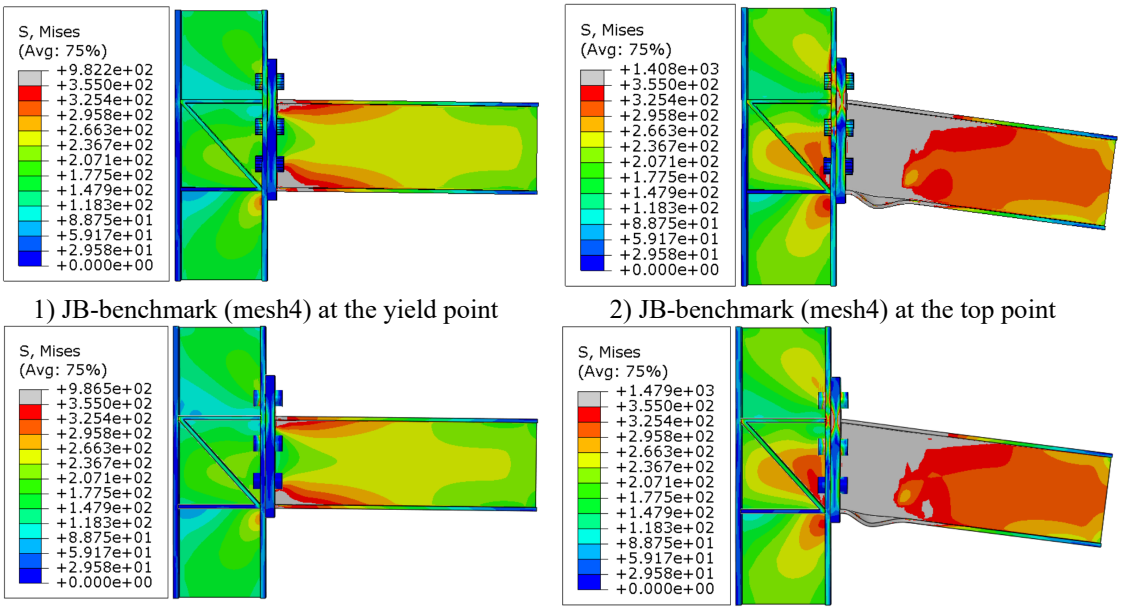

1) JB-benchmark (mesh4) at the yield point 2) JB-benchmark (mesh4) at the top point

3) JB-benchmark (mesh2) at the yield point 4) JB-benchmark (mesh2) at the top point

Figure. 34 Stress contour of benchmark joints at different points of the moment-rotation curve

Table. 3 Nonlinear analysis result of benchmark joints

Model Name	M_y (kN*m)	M_u (kN*m)	θ_y (rad)	θ_u (rad)	S (kN*m/rad)
JB-benchmark (mesh4)	**103.96**	**134.08**	**0.0053**	**0.099**	**17071**
JB-benchmark (mesh2)	92.38	135.92	0.0031	0.083	19097

4.2. Comparison of rotational stiffness (S)

According to BS EN 1993-1-3 (British Standards Institute, 2005), the beam-to-column joints can be classified into three categories, rigid joints, semi-rigid joints, and nominally pinned joints, by rotational stiffness (S). In this moment-resisting frame, the limits of these categories are calculated and shown in Table. 4.

Table. 4 Classification of joints by rotational stiffness

Joint Category	Category Limit
Rigid joints (Zone 1)	$S \geq 22486$ kN*m/rad
Semi-rigid joints (Zone 2)	450 kN*m/rad $< S <$ 22486 kN*m/rad
Nominally pinned joints (Zone 3)	$S \leq 450$ kN*m/rad

After being normalised by the rotational stiffness of JB-benchmark (mesh4), the results of all models are displayed in Figure. 35. None of the optimised joints is classified as nominally pinned joints. Most of these joints are classified as rigid joints and can provide a larger rotational stiffness than the benchmark joint. The comparison among optimised joints is presented in the following paragraphs.

When the length and height of the connection domain and stiffness domain remain unchanged, the variation in weights of the loading cases leads to at most a 195.8% increase in S. Only one optimised joint under the SEA criterion has the highest rotation stiffness, when these geometry variables are constant.

The decrease in the connection domain length (L_c) leads to the increase in S observed in most of the optimised joints. With the increase in connection domain volume, this increase in S decreases in the LC and SE criterion. If the connection domain volume is higher than a certain value, this decrease in L_c may cause a decrease in S, which can be observed in all criteria. 50.0% decrease in L_c can cause at most 115.1% increase in S. For different combinations of the connection volume and H_c, the average increases of S in the LC, SE, and SEA criterion caused by 50.0% decrease in L_c, are 59.3%, 23.1% and 10.2%, respectively.

The increase in the connection domain height (H_c) leads to the increase in S found in all optimised joints. With the increase in connection domain volume, this increase in S becomes more obvious. This increase in S is relatively remarkable in the LC criterion. 50.0% increase in H_c can cause at most 456.5% increase in S. For different combinations of the connection domain volume and L_c, the average increases of S in the LC, SE, and SEA criterion, caused by a 50.0% increase in H_c, are 168.0%, 181.4% and 76.2%, respectively.

The increase in the connection domain volume leads to the increase in S witnessed by all these joints. Generally, this increase in S is more remarkable in the SE criterion. 85.7% increase in this volume can cause at most 1230.3% increase in S. For different combinations of L_c and H_c, the average increases of S in LC, SE, and SEA criterion, caused by an 85.7% increase in this volume, are 313.6%, 670.2% and 277.7%, respectively.

Overall, the most effective strategy to increase the rotation stiffness (S) is to increase the connection domain volume. SE criterion is the best criterion in the improvement of S, since rotation stiffness is more sensitive to the change of other factors, except the length of the connection domain (L_c). SEA criterion is the worst criterion since rotation stiffness is less sensitive to the change of the other factors.

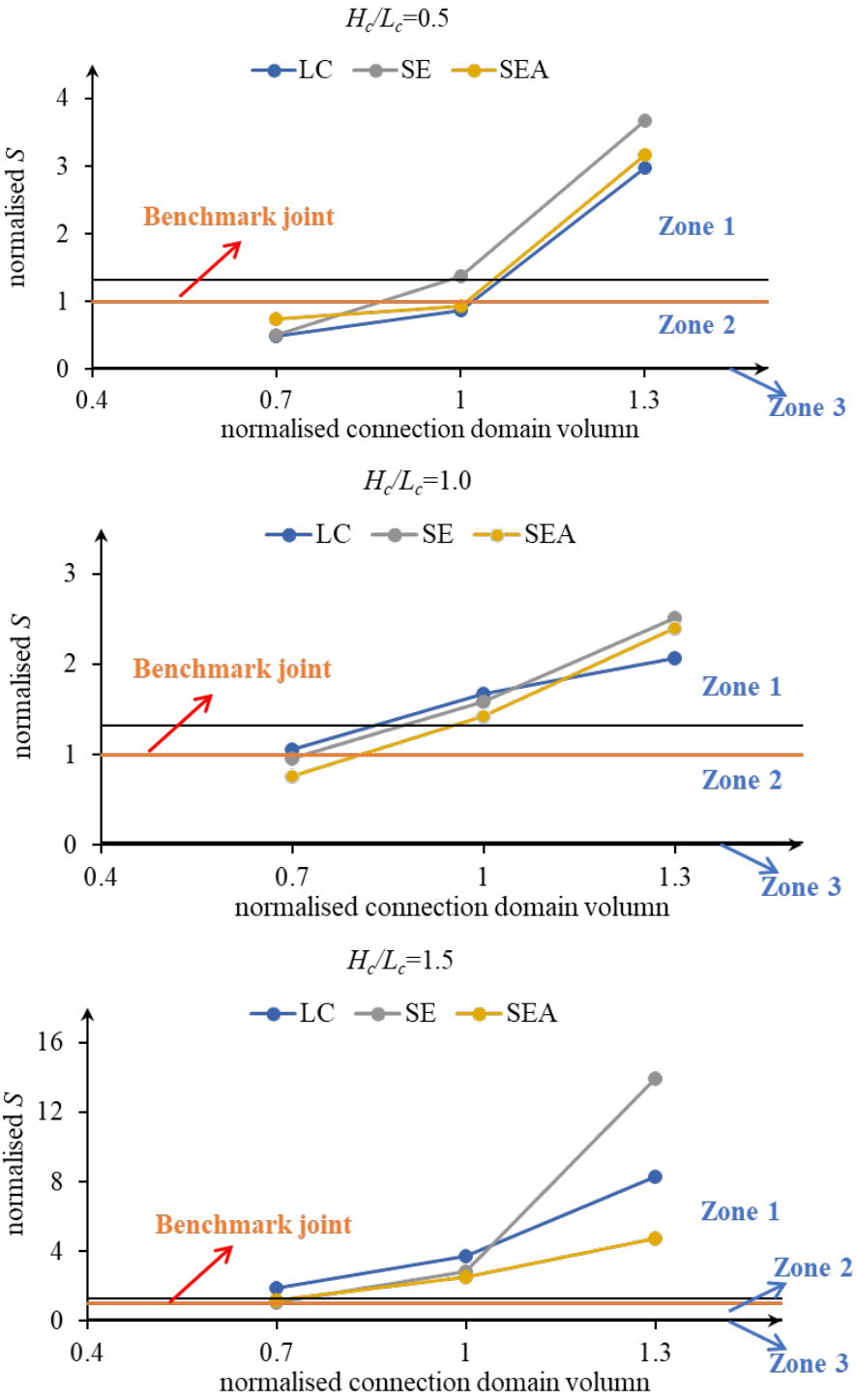

Figure. 35 The variation in the S along with the change of the connection domain volume at different height-to-length ratios (H_c/L_c)

4.3. Comparison of bending moment at yield point (M_y)

After being normalised by the result from JB-benchmark (mesh4), the results of all models are displayed in Figure. 36. The stress contours when joints reach the yield point are displayed in Figure. 37. It should highlight that the grey regions in columns and beams do not indicate that material in these regions yields, since the material property in optimised domains (connections and stiffeners) and non-optimised domains (columns and beams) is different. Conversely, the grey regions in optimised domains indicate that

material in these regions yields.

Form Figure. 36, compared with the benchmark joint, only a few of the optimised joints provide a larger M_y. A huge decrease in θ_y can be observed in many of these joints. From Figure. 37, generally, only material at the slenderer legs yields. The comparison among optimised joints is presented in the following paragraphs.

When the length and height of the connection domain and stiffness domain remain unchanged, the variation in weights of the loading cases leads to at most a 53.6% increase in M_y. Only one optimised joint under the SEA criterion has the highest M_y, when these geometry variables are constant.

The decrease in the connection domain length (L_c) leads to the decrease in M_y observed in most of the optimised joints. 50.0% decrease in L_c can cause at most a 28.4% decrease in M_y in some joints and at most a 26.9% increase in M_y in other joints. For different combinations of the connection domain volume and H_c, the average decrease in M_y in the SE and SEA criterion, caused by a 50.0% decrease in L_c, are 6.6% and 0.2%, respectively.

Similarly, the increase in the connection domain height (H_c) leads to the decrease in M_y found in most of these joints. With the increase in connection domain volume, this decrease in M_y becomes less obvious. A 50.0% increase in H_c can cause at most a 22.7% decrease in M_y in some joints and at most a 27.1% increase in M_y in other joints. For different combinations of the connection domain volume and L_c, a 50.0% increase in H_c can cause the 3.2% and 11.0% average decreases of M_y in the SE and SEA criterion, respectively.

The increase in the connection domain volume leads to the increase in M_y witnessed by all these joints. Generally, this increase in M_y is more remarkable in the SE criterion. An 85.7% increase in this volume can cause at most a 220.2% increase in M_y. For different combinations of L_c and H_c, the average increases of M_y in the LC, SE, and SEA criterion, caused by an 85.7% increase in this volume, are 157.8%, 199.3%, and 183.8%, respectively.

Overall, the most effective strategy to increase M_y is to increase the connection domain volume. It is difficult to distinguish the most critical criterion through the comparison of M_y since there is no remarkable difference in the sensitivity of M_y to the change of the other factors.

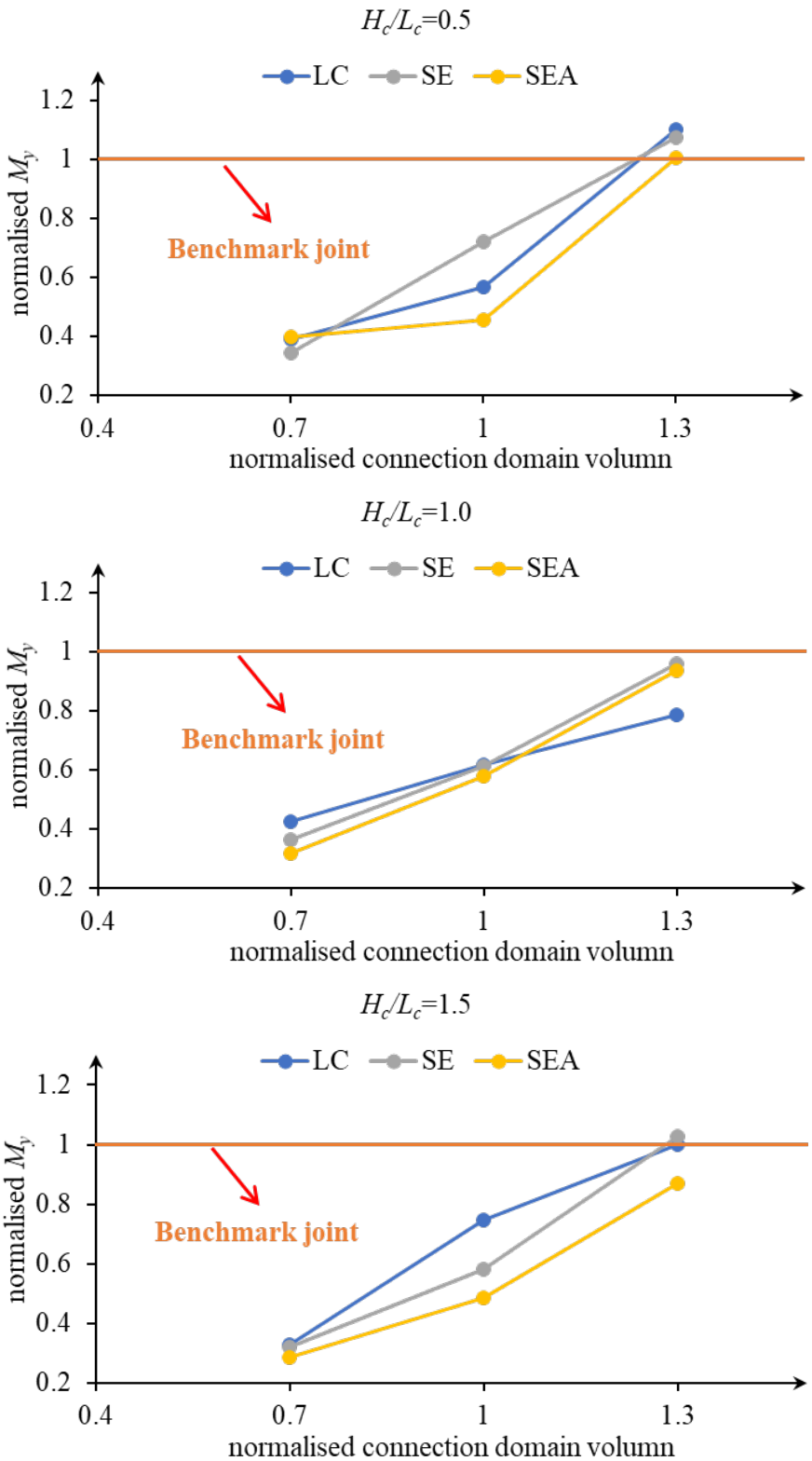

Figure. 36 The variation in the M_y along with the change of the connection domain volume at different height-to-length ratios (H_c/L_c)

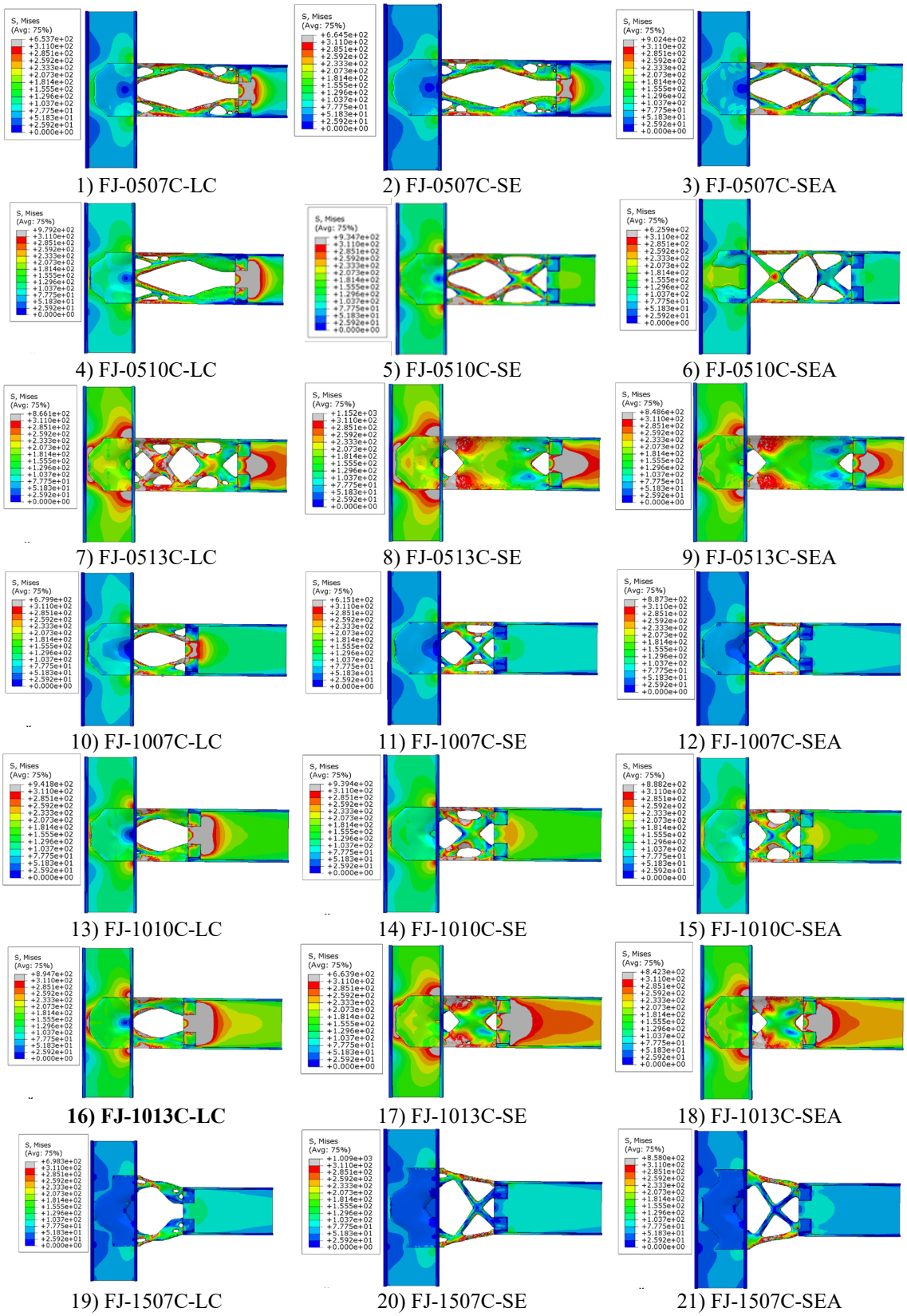

Figure. 37 Stress contours of optimised joints at the yield point of the moment-rotation curve

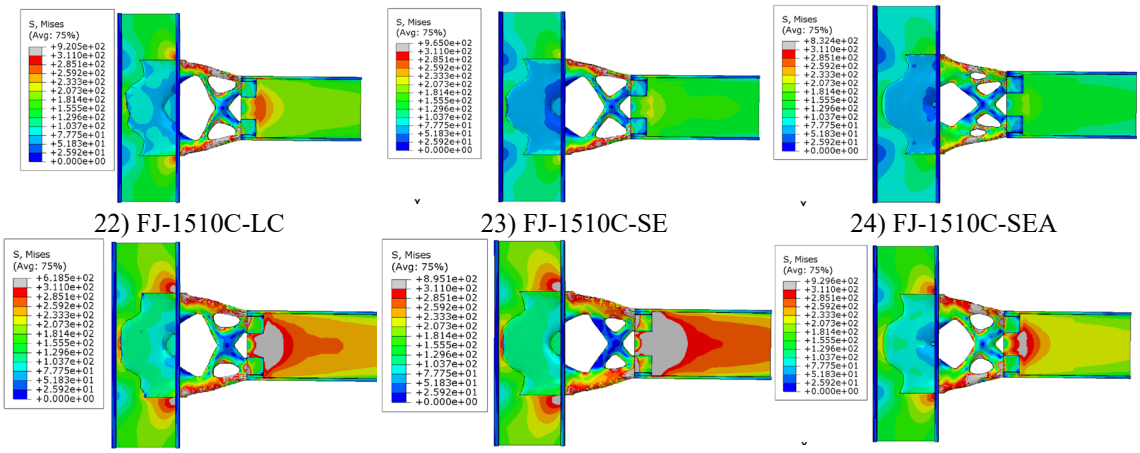

22) FJ-1510C-LC 23) FJ-1510C-SE 24) FJ-1510C-SEA

25) FJ-1513C-LC 26) FJ-1513C-SE 27) FJ-1513C-SEA

Figure. 37 Stress contours of optimised joints at the yield point of the moment-rotation curve (continuous)

4.4. Comparison of rotation angle at yield point (θ_y)

After being normalised by the result from JB-benchmark (mesh4), the results of all models are displayed in Figure. 38. Form Figure. 38, compared with the benchmark joint, most of the optimised joints cannot provide a larger θ_y. A huge decrease in θ_y can be observed in many of these joints. The comparison among optimised joints is presented in the following paragraphs.

When the length and height of the connection domain and stiffness domain remain unchanged, the variation in weights of the loading cases leads to at most a 183.6% increase in θ_y. Only one optimised joint under the SE criterion has the highest rotation stiffness when these geometry variables are constant.

The decrease in the connection domain length (L_c) leads to the decrease in θ_y observed in most of the optimised joints. If the connection domain volume is larger than a certain value, this decrease in L_c may cause the increase in θ_y, which can be observed in joints in all criteria. A 50% decrease in L_c can cause at most a 55.6% decrease in θ_y in some joints and at most a 24.7% increase in θ_y in other joints. For different combinations of the connection volume and H_c, the average decreases of θ_y in the LC, SE, and SEA criterion, caused by a 50% decrease in L_c, are 28.5%, 17.0%, and 9.9%, respectively.

Similarly, the increase in the connection domain height (H_c) leads to the decrease in θ_y found in all optimised joints. Generally, with the increase in connection domain volume, this decrease in θ_y becomes more severe. A 50% increase in H_c can cause at most a 69.8% decrease in θ_y in some joints and at most a 46.8% increase in θ_y in other joints. For different combinations of the connection domain volume and L_c, the average decreases of θ_y in the LC, SE, and SEA criterion, caused by a 50% increase in H_c, are 54.2%, 44.4%, and 39.2%, respectively.

The increase in the connection domain volume causes the decrease in θ_y witnessed by many of these joints. When H_c/L_c equals 1.0 and 1.5, θ_y becomes less sensitive to the change of this volume. Generally, this decrease in θ_y is more severe in the SE criterion. An 85.7% increase in this volume can cause at most a 63.4% decrease in θ_y. For different combinations of L_c and H_c, the average decreases of θ_y in the LC and SE criterion, caused by an 85.7% increase in this volume, are 4.7% and 35.6%, respectively.

Overall, the decrease in θ_y seems to be unavoidable. The variation of H_c is more critical, which can lead to a severe decrease in θ_y in some joints. It is difficult to distinguish the most fateful criterion through the comparison of θ_y, due to the lack of clear evidence, which indicates that more combinations of L_c, H_c, the connection domain volume, and different criteria.

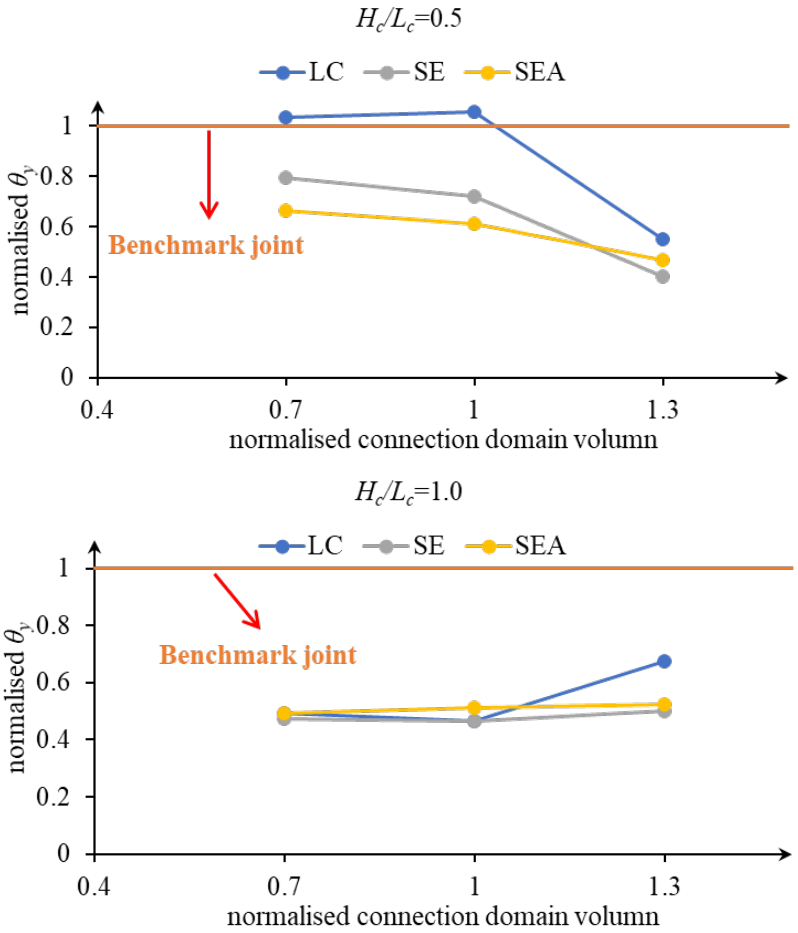

Figure. 38 The variation in the θ_y along with the change of the connection domain volume at different height-to-length ratios (H_c/L_c)

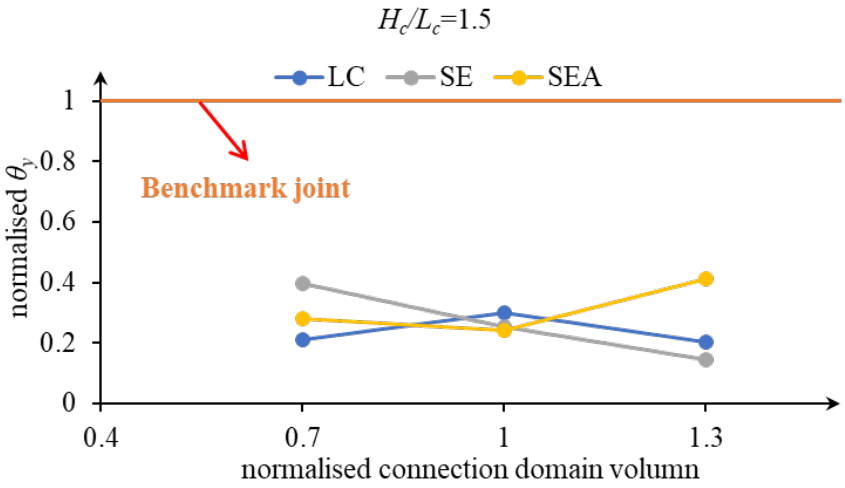

Figure. 38 The variation in the θ_y along with the change of the connection domain volume at different height-to-length ratios (H_c/L_c) (continuous)

4.5. Comparison of bending moment capacity (M_u)

According to BS EN 1993-1-3 (British Standards Institute, 2005), the beam-to-column joints can be classified into three categories, full-strength joints, partial-strength joints, and nominally pinned joints, by design moment resistance. In this dissertation, since the bolts are not simulated by the nonlinear analysis models, the design moment resistance of optimised joints cannot be obtained. Hence, these joints are classified into these categories roughly, using the bending moment capacity (M_u). The limits of these categories are calculated based on the design plastic moment resistance of beam section and shown in Table. 5.

Table. 5 Classification of joints by strength

Joint Category	**Category Limit**
Full-strength joints (Zone 1)	$M_u \geq 92$ kN*m
Partial-strength joints (Zone 2)	23 kN*m < M_u < 92 kN*m
Nominally pinned joints (Zone 3)	$M_u \leq 23$ kN*m

After being normalised by the moment capacity of JB-benchmark (mesh4), the results of all models are displayed in Figure. 39. None of optimised joints can be classified as nominally pinned joints. Most of these joints are partial-strength joints. Compared with the result from the benchmark joint, more than half of the optimised joints cannot provide a larger moment capacity. A severe decrease in M_u can be observed in many of these joints. The comparison among optimised joints is presented in the following paragraphs.

When the length and height of the connection domain and stiffness domain remain unchanged, the variation in weights of the loading cases leads to at most an 82.1% increase in M_u. Only one optimised joint under the SEA criterion has the highest moment

capacity when these geometry variables are constant.

The decrease in the connection domain length (L_c) causes the decrease in M_u observed in many of the optimised joints. A 50% decrease in L_c can cause at most a 27.2% decrease in M_u in some joints and at most a 47.1% increase in M_u in other joints. For different combinations of the connection volume and H_c, the average decrease in M_u in the SE criterion, caused by a 50% decrease in L_c, is 5.1%, while the average increases in M_u in the LC and SEA criterion, caused by the same amount of decrease in L_c, are 25.6% and 2.7%, respectively.

The increase in the connection domain height (H_c) leads to the decrease in M_u found in most of the optimised joints. A 50% increase in H_c can cause at most a 23.1% decrease in M_u in some joints and at most an 18.7% increase in M_u in other joints. For different combinations of the connection domain volume and L_c, the average increases of M_u in the LC and SEA criterion, caused by a 50% increase in H_c, are 3.9% and 5.7%, respectively.

The increase in the connection domain volume leads to the increase in M_u witnessed by all these joints. Generally, this increase in M_u is more remarkable in the SE criterion. An 85.7% increase in this volume can cause at most a 270.4% increase in M_u. For different combinations of L_c and H_c, the average increases of M_u in the LC, SE, and SEA criterion, caused by an 85.7% increase in this volume, are 137.8%, 245.4%, and 217.0%, respectively.

Overall, the most effective strategy to increase the bending moment capacity (M_u) is to increase the connection domain volume. It is difficult to distinguish the most critical criterion through the comparison of M_u, due to the lack of clear evidence, which indicates that more combinations of L_c, H_c, the connection domain volume, and different criteria.

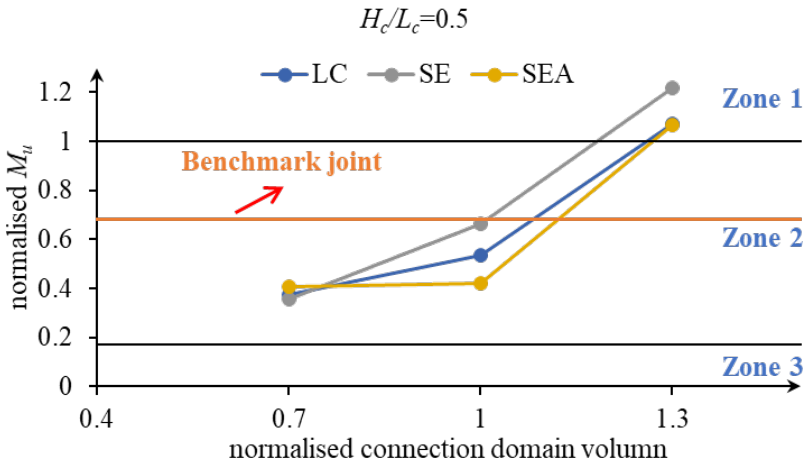

Figure. 39 The variation in the M_u along with the change of connection domain volume at different height-to-length ratios (H_c/L_c)

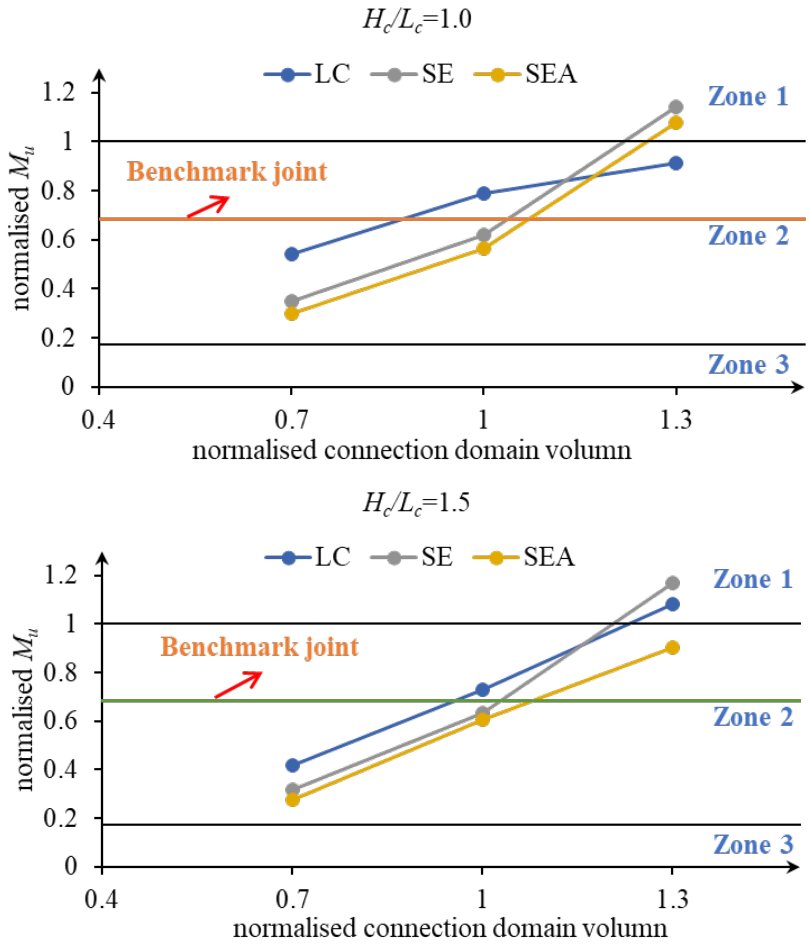

Figure. 39 The variation in the M_u along with the change of connection domain volume at different height-to-length ratios (H_c/L_c) (continuous)

4.6. Comparison of rotational capacity (θ_u)

After being normalised by the rotational capacity of JB-benchmark (mesh4), the results of all models are displayed in Figure. 40. Compared with the result from the benchmark joint, more than half of the optimised joints provide a smaller value of θ_u, while some of these joints can provide a nearly doubled rotational capacity. The comparison among optimised joints is presented in the following paragraphs.

When the length and height of the connection domain and stiffness domain remain unchanged, the variation in weights of the loading cases can cause at most a 1810.3% increase in θ_u. None of the optimised joints under the SEA criterion has the highest rotation stiffness when these geometry variables are constant.

The decrease in the connection domain length (L_c) results in the increase in θ_u observed in most of the optimised joints. A 50% decrease in L_c can cause at most a 1555.3% increase in θ_u in some joints and at most a 90.0% decrease in θ_u in other joints. For different combinations of the connection volume and H_c, the average increase in θ_u in the LC criterion, caused by a 50% decrease in L_c, is 44.6%.

The increase in the connection domain height (H_c) results in the decrease in θ_u found in the majority of the optimised joints. A 50% decrease in H_c can cause at most a 151.0% increase in θ_u in some joints and at most a 71.1% decrease in θ_u in other joints. For different combinations of the connection volume and H_c, the average decreases of θ_u in the LC and SE criterion, caused by a 50% decrease in L_c, are 49.9% and 10.9%, respectively.

The increase in the connection domain volume results in the increase in θ_u witnessed by all these joints. Generally, this increase in θ_u is more remarkable in the SE and SEA criterion. An 85.7% increase in this volume can cause at most a 1663.2% increase in θ_u. For different combinations of L_c and H_c, the average increases of θ_u in the LC, SE, and SEA criterion, caused by an 85.7% increase in this volume, are 32.0%, 529.6%, and 700.3%, respectively.

Overall, many of the optimised joints are less ductile compared with the benchmark joint. The most effective strategy to improve the ductility is to increase the connection domain volume. And it is difficult to distinguish the most critical criterion through the comparison of θ_u, due to the lack of clear evidence, which indicates that more combinations of L_c, H_c, the connection domain volume, and different criteria.

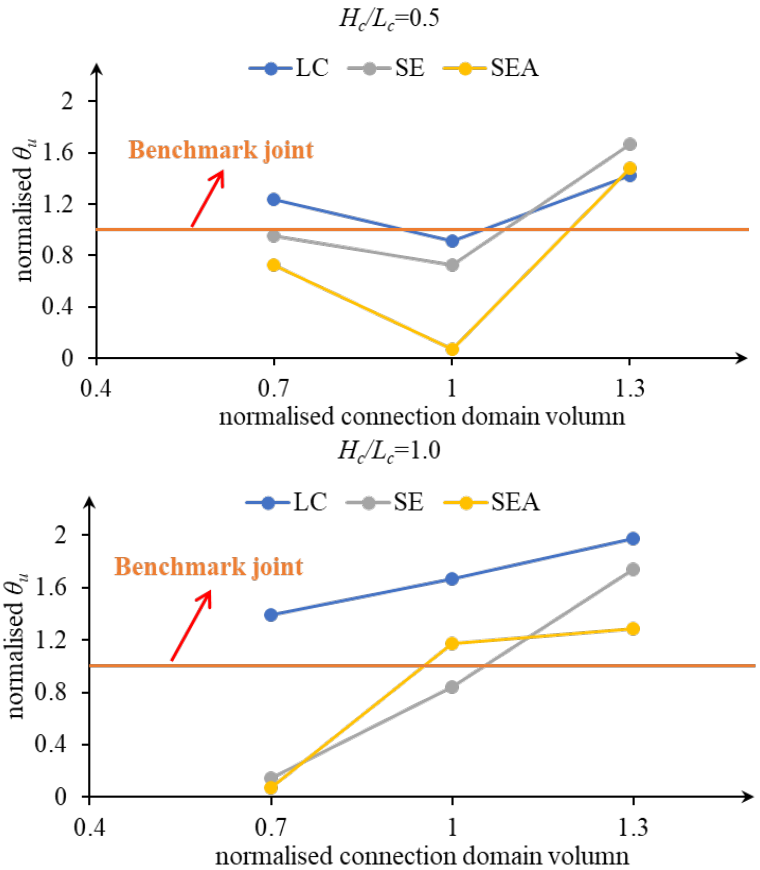

Figure. 40 The variation in the θ_u along with the change of the connection domain volume at different height-to-length ratios (H_c/L_c)

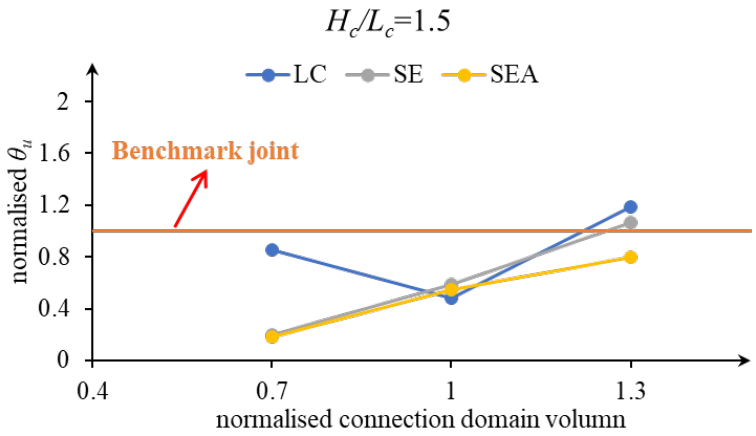

Figure. 40 The variation in the θ_u along with the change of the connection domain volume at different height-to-length ratios (H_c/L_c) (continuous)

4.7. Comparison of failure modes

The stress contours when joints reach the moment capacity are displayed in Figure. 41. It should highlight that the grey regions in columns and beams do not indicate that material in these regions yields. Conversely, these regions in stiffeners and connections indicate that material in these regions yields.

The truss-form joints, such as FJ-1010C-SE (Figure. 41 (16)), which contain slender legs, fail due to local buckling of these legs. Other joints can still fail due to the local buckling of the material in the highly compressed region.

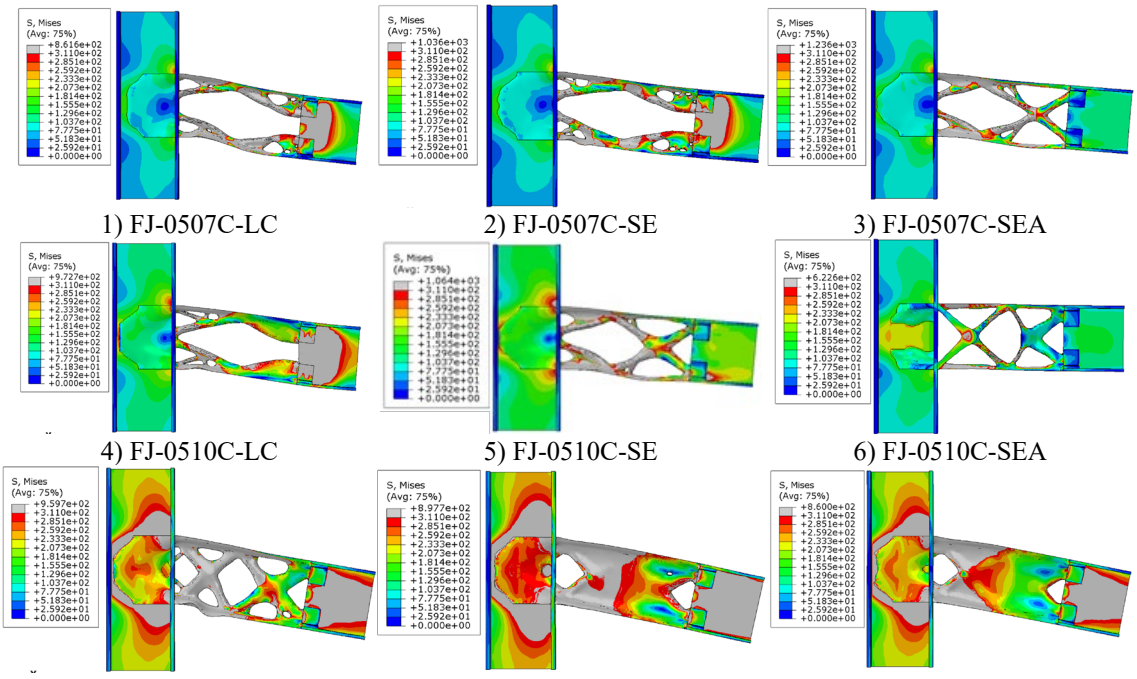

1) FJ-0507C-LC 2) FJ-0507C-SE 3) FJ-0507C-SEA

4) FJ-0510C-LC 5) FJ-0510C-SE 6) FJ-0510C-SEA

7) FJ-0513C-LC 8) FJ-0513C-SE 9) FJ-0513C-SEA

Figure. 41 Stress contours of optimised joints at the top point of the moment-rotation curve

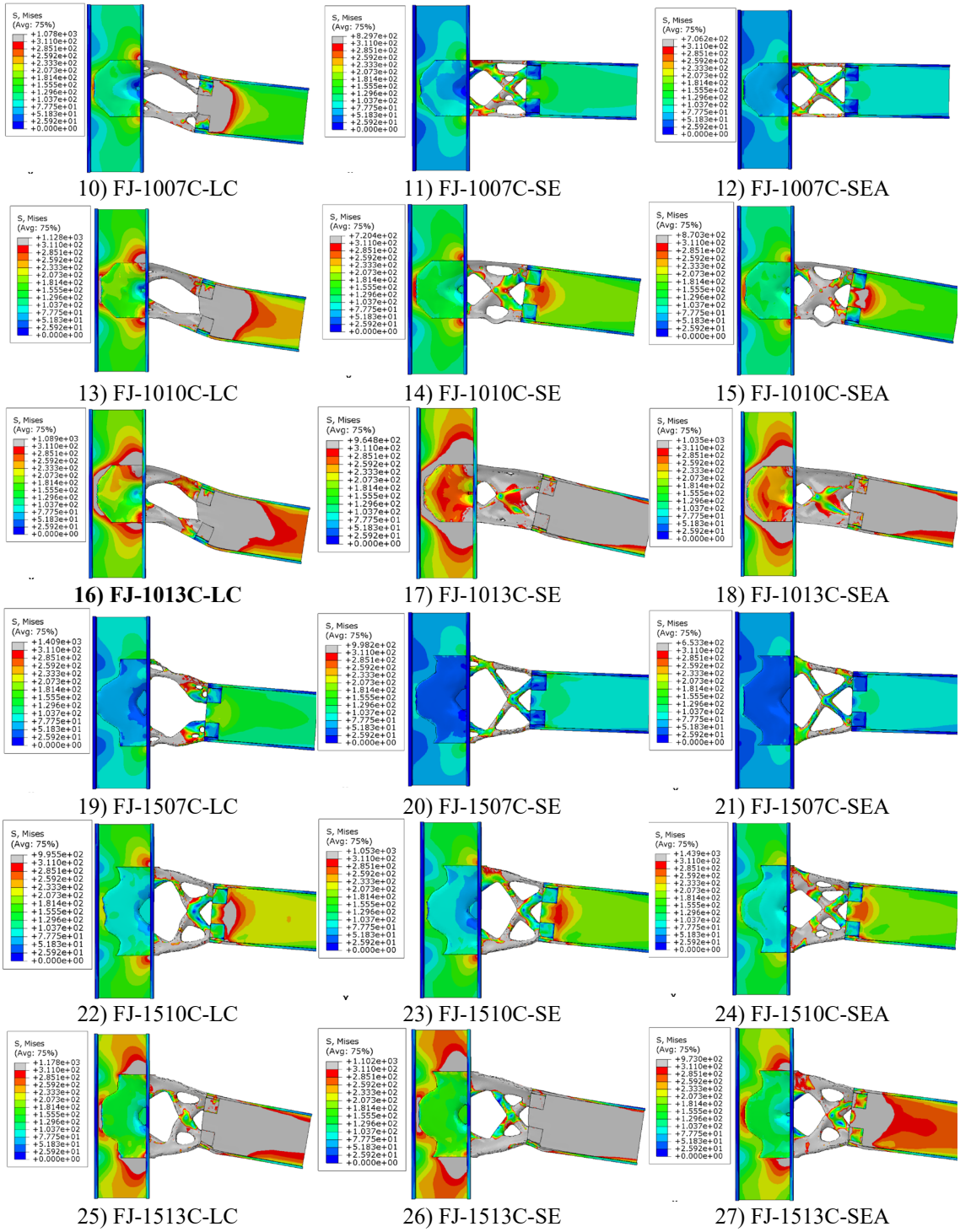

Figure. 41 Stress contours of optimised joints at the top point of the moment-rotation curve (continuous)

In conclusion, fully compared with the benchmark joint, FJ-1013C-LC, classified as a semi-rigid, full-strength joint, outshines other optimised joints. Although this joint does not have the highest bending moment capacity, it has the highest rotational capacity, which means that this joint has the highest ductility, nearly doubling the benchmark value. Consequently, considering the ductility is a critical performance parameter in construction, FJ-1013C-LC is decided as the most successful optimised joint, which will be simulated more detailly in the future. During the topology optimisation, more combinations of optimisation setups, such as L_c, H_c, the connection domain volume, and

different criteria, should be considered to explore the more critical criterion for the calculation of weights of loading cases.

5. CONCLUSIONS

Through the topology optimisation, the insignificant and significant influence factors of topology optimisation are found. Through the nonlinear analysis and comparison with the benchmark joint, the structural performance of the optimised joints is assessed. The most outstanding optimised joint, FJ-1013C-LC, is found. The key findings in this dissertation are summarised as follows:

1) When optimising the connection domain, the effect caused by the existent of stiffeners can be ignored. But considering the contribution of stiffeners to the structural performance improvement, stiffener and connection are supposed to be optimised simultaneously.
2) Without consideration of computing time, the mesh size should be as small as possible, to get the more desired optimised geometry. However, this complex geometry cannot guarantee that this joint has the best structural performance.
3) The effect of the red domain length (l_c) can be ignored if the connection domain is the focus in the topology optimisation.
4) Optimised under multiple loading cases, joints often have a more uniform performance in the specific loading condition.
5) When joints are optimised under multiple loading cases, the definition of weights of each loading condition is important and should be studied further.
6) Although the weightiness of different loading conditions may be different in practical application, it is a strategy to enrich the optimised geometry by changing these weights. There is not a generic methodology to define these weights.
7) Another effective strategy to enrich the optimised geometry is changing the length (L_c) and height (H_c) of the blue domain and the optimisation target. In this research, this target can be the blue domain volume.
8) The nonlinear analysis of each optimised joint is indispensable.
9) Generally, increase the material of the optimised joints is an effective way to improve the structural performance of these joints.
10) Changing one particular parameter in the topology optimisation cannot guarantee the improvement of all structural performance variables for the optimised joints.
11) By comprehensive considering of the structural performance, FJ-1013C-LC is decided as the most optimised beam-to-column joint.

REFERENCE

American Society for Material and Testing. (2012) *Standard terminology for additive manufacturing technologies, vol.F2792-12a.* West Conshohocken, PA, ASTM International.

Bendsøe, M. P. & Sigmund, O. (2004) *Topology optimization: theory, methods, and applications.* Berlin, Germany, Springer.

Bogue, R. (2014) 3D printing: the dawn of a new era in manufacturing? *Assembly Automation.* 33 (4), 307-311.

Bos, F., Wolfs, R., Ahmed, Z. & Salet, T. (2016) Additive manufacturing of concrete in construction: potentials and challenges of 3D concrete printing. *Virtual and Physical Prototyping.* 11 (3), 1-17.

British Standards Institute. (2005) *BS EN 1993-1-8:2005: Eurocode 3. Design of steel structures. Design of joints.* London, British Standards Institute.

Brown, D. G., Lles, D. C. (2013) *Joints in Steel Construction: Moment-Resisting Joints to Eurocode 3.* 1st edition. London, Steel Construction Institute.

Buchanan, C. & Gardner, L. (2019) Metal 3D printing in construction: A review of methods, research, applications, opportunities and challenges. *Engineering Structures.* 180, 332-348.

Ding, D., Pan, Z., Cuiuri, D. & Li, H. (2015) Wire-feed additive manufacturing of metal components: technologies, developments and future interests. *The International Journal of Advanced Manufacturing Technology.* 81 (1), 465-481.

Galjaard, S., Hofman, S., Perry, N. & Ren, S. (2015) Optimizing Structural Building Elements in Metal by using Additive Manufacturing. *Proceedings of IASS Annual Symposia.* 2015 (2), 1-12.

Galjaard, S., Hofman, S. & Ren, S. (2015) New opportunities to optimize structural designs in metal by using additive manufacturing. In: Anonymous *Advances in architectural geometry 2014.* Cham, Springer. pp. 79-93.

Gao, W., Zhang, Y., Ramanujan, D., Ramani, K., Chen, Y., Williams, C. B., Wang, C. C. L., Shin, Y. C., Zhang, S. & Zavattieri, P. D. (2015) The status, challenges, and future of additive manufacturing in engineering. *Computer-Aided Design.* 69, 65-89.

Gu, D. D., Meiners, W., Wissenbach, K. & Poprawe, R. (2012) Laser additive manufacturing of metallic components: materials, processes and mechanisms. *International Materials Reviews.* 57 (3), 133-164.

Hayley, D. (2017) *The world's first 3D printed steel bridge will be a 'living laboratory'.* Available from: https://www.imperial.ac.uk/news/182593/the-worlds-first-3d-printed-steel/ [Accessed Aug 17, 2021].

Joosten, S. K. (2015) *Printing a stainless steel bridge: An exploration of structural properties of stainless steel additive manufactures for civil engineering purposes.* Delft University of Technology.

Kyvelou, P., Slack, H., Daskalaki Mountanou, D., Wadee, M. A., Britton, T. B., Buchanan, C. & Gardner, L. (2020) Mechanical and microstructural testing of wire and arc additively manufactured sheet material. *Materials & Design.* 192, 108675.

Laghi, V., Palermo, M., Tonelli, L., Gasparini, G., Ceschini, L. & Trombetti, T. (2020) Tensile properties and microstructural features of 304L austenitic stainless steel produced by wire-and-arc additive manufacturing. *The International Journal of Advanced Manufacturing Technology.* 106 (9), 3693-3705.

Lange, J. ö, Feucht, T. & Erven, M. (2020) 3D printing with steel. *Steel Construction*. 13 (3), 144-153.

Sundaram, M. M., Kamaraj, A. B. & Kumar, V. S. (2015) Mask-less electrochemical additive manufacturing: a feasibility study. *Journal of Manufacturing Science and Engineering.* 137 (2), 1-9.

Tartaglia, R., D'Aniello, M., Campiche, A. & Latour, M. (2021) Symmetric friction dampers in beam-to-column joints for low-damage steel MRFs. *Journal of Constructional Steel Research.* 184, 106791.

Thompson, M. K., Moroni, G., Vaneker, T., Fadel, G., Campbell, R. I., Gibson, I., Bernard, A., Schulz, J., Graf, P., Ahuja, B. & Martina, F. (2016) Design for Additive

Manufacturing: Trends, opportunities, considerations, and constraints. *CIRP Annals.* 65 (2), 737-760.

Tolosa, I., Garciandía, F., Zubiri, F., Zapirain, F. & Esnaola, A. (2010) Study of mechanical properties of AISI 316 stainless steel processed by "selective laser melting", following different manufacturing strategies. *The International Journal of Advanced Manufacturing Technology.* 51 (5), 639-647.

Williams, S. W., Martina, F., Addison, A. C., Ding, J., Pardal, G. & Colegrove, P. (2016) Wire + Arc Additive Manufacturing. *Materials Science and Technology.* 32 (7), 641-647.

Wu, P., Wang, J. & Wang, X. (2016) A critical review of the use of 3-D printing in the construction industry. *Automation in Construction.* 68, 21-31.

Yun, X. & Gardner, L. (2017) Stress-strain curves for hot-rolled steels. *Journal of Constructional Steel Research.* 133, 36-46.

Zhu, C., Rasmussen, K. J. R., Yan, S. & Zhang, H. (2019) Experimental Full-Range Behavior Assessment of Bolted Moment End-Plate Connections. *Journal of Structural Engineering (New York, N.Y.).* 145 (8), 4019079.

APPENDIX A: NAMING SYSTEM FOR MODELS

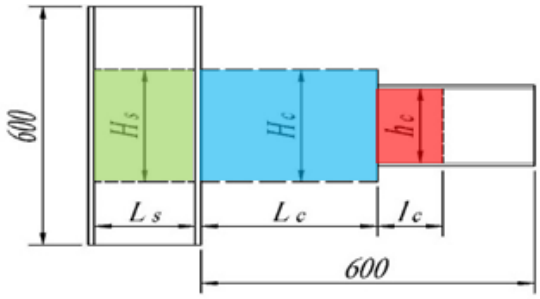

Figure. A.1 General dimension of design domains

Analysis name	Segment of model name	Meaning of element in segment
Pre-analysis (topology optimisation analysis)	'P'	• The model belongs to pre-analysis
	'xxxx' + 'MS', 'PS' or 'PM'	• **Number part:** 1) The first two number means the height to length ratio (H_c/L_c) of green domain. 2) The last two number means the height to length ratio (h_c/l_c) of red domain. • **Letter part:** 1) MS means the model is optimised under a combination of hogging moment and shear force. 2) PS means the model is optimised under pure shear force. 3) PM means the model is optimised under pure hogging moment.
	'SN', 'SG' or 'SD' + 'M4' or 'M8'	• **First part:** 1) SN means there is not a stiffener in the column. 2) SG means the geometry of stiffener is given and that there is only one individual design domain, the connection domain. 3) SD means there are two individual design domains, stiffener domain and connection domain. • **Second part:** 1) M4 means the mesh size of design domain is equal to 4. 2) M8 means the mesh size of design domain is equal to 8.
Formal analysis (topology optimisation analysis) **& Nonlinear analysis**	'FJ'	• The model belongs to formal analysis and has a stiffener domain located in the column.
	'xxxx' + 'MS', 'PS', 'PM' or 'C'	• **Number part:** 1) The first two number means the height to length ratio (H_c/L_c) of green domain. 2) The last two number means the normalised volume of optimised connection domain ($V_c^{normalised}$) • **Letter part:** 1) MS means the model is optimised under a combination of hogging moment and shear force. 2) PS means the model is optimised under pure shear force. 3) PM means the model is optimised under pure hogging moment. 4) C means the model is optimised under multiple loading cases.
	'N', 'LC', 'SE' or 'SEA'	• N means the model is optimised under single loading case, without the need of weights of loading cases. • LC means the weights are defined according to load control criterion. • SE means the weights are defined according to SE criterion. • SEA means the weights are defined according to SEA criterion.

APPENDIX B: DETAIL INFORMATION FOR TOPOLOGY-OPTIMISATION MODELS

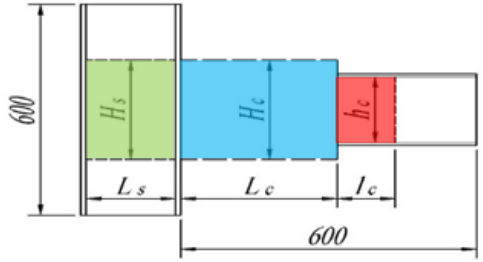

Figure. B.1 General dimension of design domains

Note:

1) T_s is the thickness of the green domain.
2) T_c is the thickness of the blue domain.
3) t_c is the thickness of the red domain.
4) M is the magnitude of the reaction moment at the column flange
5) V is the magnitude of the downward shear force at the column flange.
6) M_{pl} is the plastic moment resistance of the beam section.
7) R_v is the shear force resistance of the beam section.

Table B.1 Detail information for models in pre-analysis

Model Name	Stiffener Domain (Green Domain)				Connection Domain								Optimisation Target	Mesh Size	Loading Condition	
					Blue Domain				Red Domain							
	L_s (mm)	H_s (mm)	T_s (mm)	Optimisation Target	L_c (mm)	H_c (mm)	T_c (mm)	H_c/L_c	l_c (mm)	h_c (mm)	t_c (mm)	h_c/l_c			M/M_{pl}	V/R_v
P-0707MS-SDM4	181.2	203.2	98.2	0.5	290.3	203.2	101.8	0.7	268.0	187.6	63.75	0.7	0.5	4	1.88	0.67
P-0710MS-SDM4	181.2	203.2	98.2	0.5	290.3	203.2	101.8	0.7	187.6	187.6	63.75	1.0	0.5	4	1.88	0.67
P-0710MS-SDM8	181.2	203.2	98.2	0.5	290.3	203.2	101.8	0.7	187.6	187.6	63.75	1.0	0.5	8	1.88	0.67
P-0714MS-SDM4	181.2	203.2	98.2	0.5	290.3	203.2	101.8	0.7	131.3	187.6	63.75	1.4	0.5	4	1.88	0.67
P-1010MS-SDM4	181.2	203.2	98.2	0.5	203.2	203.2	101.8	1.0	187.6	187.6	63.75	1.0	0.5	4	1.88	0.67
P-1010MS-SDM8	181.2	203.2	98.2	0.5	203.2	203.2	101.8	1.0	187.6	187.6	63.75	1.0	0.5	8	1.88	0.67
P-1410MS-SDM4	181.2	290.3	98.2	0.5	203.2	290.3	101.8	1.4	187.6	187.6	63.75	1.0	0.5	4	1.00	0.00
P-1410MS-SDM8	181.2	290.3	98.2	0.5	203.2	290.3	101.8	1.4	187.6	187.6	63.75	1.0	0.5	8	1.00	0.00
P-0738PS-SNM4	181.2	203.2	98.2	0.5	290.3	203.2	101.8	0.7	50.0	187.6	63.75	3.8	0.5	4	0.00	1.00
P-0738PS-SGM4	181.2	203.2	98.2	0.5	290.3	203.2	101.8	0.7	50.0	187.6	63.75	3.8	0.5	4	0.00	1.00
P-0738PS-SDM4	181.2	203.2	98.2	0.5	290.3	203.2	101.8	0.7	50.0	187.6	63.75	3.8	0.5	4	0.00	1.00
P-0738MS-SNM4	181.2	203.2	98.2	0.5	290.3	203.2	101.8	0.7	50.0	187.6	63.75	3.8	0.5	4	1.88	0.67
P-0738MS-SGM4	181.2	203.2	98.2	0.5	290.3	203.2	101.8	0.7	50.0	187.6	63.75	3.8	0.5	4	1.88	0.67
P-0738MS-SDM4	181.2	203.2	98.2	0.5	290.3	203.2	101.8	0.7	50.0	187.6	63.75	3.8	0.5	4	1.88	0.67

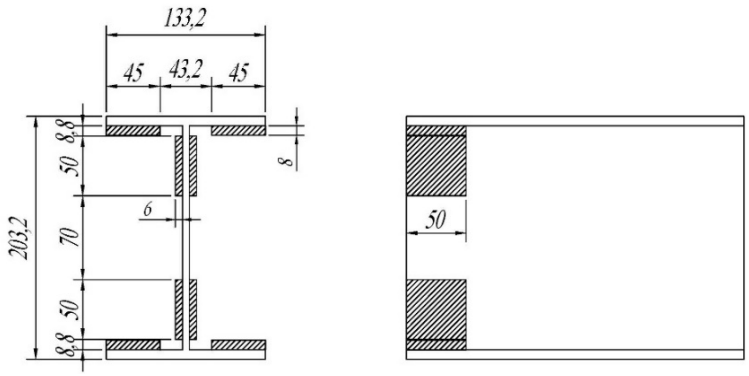

Figure. B.2 Dimension of the red design domain in formal analysis

Note:

1) For MS, M/M_{pl} equals 0.76 while V/R_v equals 0.50.
2) For PS, M/M_{pl} equals 0 while V/R_v equals 1.00.
3) For PM, M/M_{pl} equals 1.00 while V/R_v equals 0.
4) Unlike the pre-analysis, the geometry of the red design domain in formal analysis remains unchanged and is shown in Figure. B.2.

Table B.2 Detail information for models in formal analysis

Model Name	Stiffener Domain (Green Domain)				Connection Domain (Blue Domain)					Mesh Size	Weights of Loading Conditions					
											Stiffener Domain			Connection Domain		
	L_s (mm)	H_s (mm)	T_s (mm)	$V_s^{normalised}$	L_c (mm)	H_c (mm)	T_c (mm)	H_c/L_c	$V_c^{normalised}$		MS	PS	PM	MS	PS	PM
FJ-0507MS-N	181.2	203.2	98.2	1.0	406.4	203.2	101.8	0.5	0.7	4						
FJ-0507PS-N	181.2	203.2	98.2	1.0	406.4	203.2	101.8	0.5	0.7	4						
FJ-0507PM-N	181.2	203.2	98.2	1.0	406.4	203.2	101.8	0.5	0.7	4						
FJ-0507C-LC	181.2	203.2	98.2	1.0	406.4	203.2	101.8	0.5	0.7	4	1.0000	1.0000	1.0000	1.0000	1.0000	1.0000
FJ-0507C-SE	181.2	203.2	98.2	1.0	406.4	203.2	101.8	0.5	0.7	4	0.4224	0.4331	0.1445	0.4224	0.4331	0.1445
FJ-0507C-SEA	181.2	203.2	98.2	1.0	406.4	203.2	101.8	0.5	0.7	4	0.0061	0.4902	0.0036	0.2433	0.1843	0.0724
FJ-0510C-LC	181.2	203.2	98.2	1.0	406.4	203.2	101.8	0.5	1.0	4	1.0000	1.0000	1.0000	1.0000	1.0000	1.0000
FJ-0510C-SE	181.2	203.2	98.2	1.0	406.4	203.2	101.8	0.5	1.0	4	0.4224	0.4331	0.1445	0.4224	0.4331	0.1445
FJ-0510C-SEA	181.2	203.2	98.2	1.0	406.4	203.2	101.8	0.5	1.0	4	0.0061	0.4902	0.0036	0.2433	0.1843	0.0724
FJ-0513C-LC	181.2	203.2	98.2	1.0	406.4	203.2	101.8	0.5	1.3	4	1.0000	1.0000	1.0000	1.0000	1.0000	1.0000
FJ-0513C-SE	181.2	203.2	98.2	1.0	406.4	203.2	101.8	0.5	1.3	4	0.4224	0.4331	0.1445	0.4224	0.4331	0.1445
FJ-0513C-SEA	181.2	203.2	98.2	1.0	406.4	203.2	101.8	0.5	1.3	4	0.0061	0.4902	0.0036	0.2433	0.1843	0.0724

Table B.2 Detail information for models in formal analysis (continuous)

Model Name	Stiffener Domain (Green Domain)				Connection Domain (Blue Domain)					Mesh Size	Weights of Loading Conditions					
											Stiffener Domain			Connection Domain		
	L_s (mm)	H_s (mm)	T_s (mm)	$V_s^{normalised}$	L_c (mm)	L_s (mm)	H_s (mm)	T_s (mm)	$V_s^{normalised}$		MS	PS	PM	MS	PS	PM
FJ-1007MS-N	181.2	203.2	98.2	1.0	203.2	203.2	101.8	1.0	0.7	4						
FJ-1007PS-N	181.2	203.2	98.2	1.0	203.2	203.2	101.8	1.0	0.7	4						
FJ-1007PM-N	181.2	203.2	98.2	1.0	203.2	203.2	101.8	1.0	0.7	4						
FJ-1007C-LC	181.2	203.2	98.2	1.0	203.2	203.2	101.8	1.0	0.7	4	1.0000	1.0000	1.0000	1.0000	1.0000	1.0000
FJ-1007C-SE	181.2	203.2	98.2	1.0	203.2	203.2	101.8	1.0	0.7	4	0.1843	0.7292	0.0865	0.1843	0.7292	0.0865
FJ-1007C-SEA	181.2	203.2	98.2	1.0	203.2	203.2	101.8	1.0	0.7	4	0.0061	0.4903	0.0036	0.1166	0.3328	0.0506
FJ-1010C-LC	181.2	203.2	98.2	1.0	203.2	203.2	101.8	1.0	1.0	4	1.0000	1.0000	1.0000	1.0000	1.0000	1.0000
FJ-1010C-SE	181.2	203.2	98.2	1.0	203.2	203.2	101.8	1.0	1.0	4	0.1843	0.7292	0.0865	0.1843	0.7292	0.0865
FJ-1010C-SEA	181.2	203.2	98.2	1.0	203.2	203.2	101.8	1.0	1.0	4	0.0061	0.4903	0.0036	0.1166	0.3328	0.0506
FJ-1013C-LC	181.2	203.2	98.2	1.0	203.2	203.2	101.8	1.0	1.3	4	1.0000	1.0000	1.0000	1.0000	1.0000	1.0000
FJ-1013C-SE	181.2	203.2	98.2	1.0	203.2	203.2	101.8	1.0	1.3	4	0.1843	0.7292	0.0865	0.1843	0.7292	0.0865
FJ-1013C-SEA	181.2	203.2	98.2	1.0	203.2	203.2	101.8	1.0	1.3	4	0.0061	0.4903	0.0036	0.1166	0.3328	0.0506
FJ-1507MS-N	181.2	304.8	98.2	1.0	203.2	304.8	101.8	1.5	0.7	4						
FJ-1507PS-N	181.2	304.8	98.2	1.0	203.2	304.8	101.8	1.5	0.7	4						
FJ-1507PM-N	181.2	304.8	98.2	1.0	203.2	304.8	101.8	1.5	0.7	4						
FJ-1507C-LC	181.2	304.8	98.2	1.0	203.2	304.8	101.8	1.5	0.7	4	1.0000	1.0000	1.0000	1.0000	1.0000	1.0000
FJ-1507C-SE	181.2	304.8	98.2	1.0	203.2	304.8	101.8	1.5	0.7	4	0.2661	0.6187	0.1152	0.2661	0.6187	0.1152
FJ-1507C-SEA	181.2	304.8	98.2	1.0	203.2	304.8	101.8	1.5	0.7	4	0.0168	0.4733	0.0099	0.1580	0.2792	0.0628
FJ-1510C-LC	181.2	304.8	98.2	1.0	203.2	304.8	101.8	1.5	1.0	4	1.0000	1.0000	1.0000	1.0000	1.0000	1.0000
FJ-1510C-SE	181.2	304.8	98.2	1.0	203.2	304.8	101.8	1.5	1.0	4	0.2661	0.6187	0.1152	0.2661	0.6187	0.1152
FJ-1510C-SEA	181.2	304.8	98.2	1.0	203.2	304.8	101.8	1.5	1.0	4	0.0168	0.4733	0.0099	0.1580	0.2792	0.0628
FJ-1513C-LC	181.2	304.8	98.2	1.0	203.2	304.8	101.8	1.5	1.3	4	1.0000	1.0000	1.0000	1.0000	1.0000	1.0000
FJ-1513C-SE	181.2	304.8	98.2	1.0	203.2	304.8	101.8	1.5	1.3	4	0.2661	0.6187	0.1152	0.2661	0.6187	0.1152
FJ-1513C-SEA	181.2	304.8	98.2	1.0	203.2	304.8	101.8	1.5	1.3	4	0.0168	0.4733	0.0099	0.1580	0.2792	0.0628